

ALTERATION OF MAGNETIC MINERALS IN 2017 BASALTIC TUFF DRILL
CORES FROM SURTSEY VOLCANO, ICELAND,
50 YEARS AFTER ERUPTION

by

Joshua M. Marquardt

A thesis submitted to the faculty of
The University of Utah
in partial fulfillment of the requirements for the degree of

Master of Science

Department of Geology and Geophysics

The University of Utah

August 2020

Copyright © Joshua M. Marquardt 2020

All Rights Reserved

The University of Utah Graduate School

STATEMENT OF THESIS APPROVAL

The thesis of Joshua Marquardt
has been approved by the following supervisory committee members:

<u>Peter C. Lippert</u>	, Chair	<u>06/13/2020</u> Date Approved
<u>Marie D. Jackson</u>	, Member	<u>06/13/2020</u> Date Approved
<u>Sarah Lambart</u>	, Member	<u>06/13/2020</u> Date Approved

and by Thure Cerling, Chair/Dean of

the Department/College/School of Geology and Geophysics

and by David B. Kieda, Dean of The Graduate School.

ABSTRACT

Oceanic basalt is rich in magnetite and titanomagnetite, and as one of our principal archives for studying the Earth's magnetic field, the magnetic properties of basaltic rocks are a keystone of the plate tectonic theory. Titanium substitution and low-temperature oxidation (maghemitization) are ubiquitous alteration mechanisms that can change and can even corrupt the magnetic properties of remanence carrying iron oxides in oceanic basalt. In this study, we characterize the tempo of natural magnetic mineral alteration over decadal timescales using drill cores acquired in 2017 from Surtsey Volcano, Iceland. We characterize the alteration of the magnetic minerals in Surtsey deposits over the 50-year time window since eruptions terminated and situate our magnetic mineral results within the context of volcanic glass alteration. We distinguish seven structural and alteration zones that span the subaerial, submarine, and sub-seafloor deposits of the Surtur vent at Surtsey volcano. We use thin section scans to describe alteration features of the basaltic tuff, measure thermomagnetic curves to characterize the composition of the magnetic remanence carriers, measure first-order reversal curve (FORC) diagrams to diagnose the magnetic domain state, and use alternating-field demagnetization to assess the directional fidelity of magnetization. Near the cool pre-eruptive seafloor underlying the volcano at 181 m below surface, in a zone of least alteration, we find fresh-to-very weakly-altered volcanic glass pyroclasts in thin sections and uniaxial and cubic stable single domain magnetites that are the principal magnetic

remanence carriers. In the six other zones, we observe highly-vesicular glass and glass pyroclasts with palagonitized rinds indicative of higher rates of alteration. The magnetic minerals in these same six zones are cubic to isotropic stable single domain titanomagnetite, titanomaghemite, or both. Our results suggest that the magnetic properties of magnetic remanence carrying iron oxides in oceanic basalts can change over a few decades through fluid-rock interactions and elevated temperatures as they undergo alteration through Ti^{4+} substitution and maghemitization. It is possible that the maghemite-induced cracking of the magnetite crystal surface provides conduits into the more reduced cores of each iron oxide grain, thereby accelerating the redistribution of Fe^{2+} through very fine-scale fluid-rock interactions.

TABLE OF CONTENTS

ABSTRACT.....	iii
LIST OF FIGURES	vi
ACKNOWLEDGEMENTS	vii
1 INTRODUCTION	1
2 GEOLOGIC SETTING	6
3 MATERIALS AND METHODS.....	12
3.1 Core Material and Reference Samples.....	12
3.2 Petrographic Observations	13
3.3 Rock Magnetic Measurements.....	14
3.4 Weak-Field Magnetic Measurements	14
3.5 High-Field Magnetic Measurements.....	16
4 RESULTS	21
4.1 Petrographic and Material Descriptions	21
4.2 Magnetic Susceptibility	23
4.3 Paleomagnetism	25
4.4 High-Field Magnetic Remanence	27
5 DISCUSSION	38
5.1 Petrographic and Material Descriptions.....	38
5.2 Paleomagnetism of Core SE-02b	40
5.3 Magnetic Mineral Composition and its Variability	41
5.4 Magnetic Domain State and its Variability.....	46
5.5 Magnetic Mineral Alteration and its Variations	50
6 CONCLUSIONS.....	54
APPENDIX.....	59
REFERENCES	62

LIST OF FIGURES

Figures

1 Maps showing drilling operations at Surtsey volcano, Iceland	9
2 Interpretive, diagrammatic cross-section of Surtsey	10
3 Comparisons of the 1979 and 2017 cored Surtsey boreholes	11
4 Petrographic thin section scans	31
5 Bulk magnetic properties	33
6 Results from continuous $\kappa(T)$ curves	34
7 Results from progressive $\kappa(T)$ curves	35
8 Orthogonal vector plots of demagnetization results	36
9 First-order reversal curve (FORC) diagrams	37
10 Stereonet showing paleomagnetism of samples from Core SE-02b	53

ACKNOWLEDGEMENTS

I am eternally grateful for the opportunity to pursue my graduate studies in The Department of Geology and Geophysics at The University of Utah and I want to extend my gratitude to the many people who have contributed to my success here at the U.

First and foremost, I express my deep and sincere appreciation to my committee members: Dr. Peter Lippert, Dr. Marie Jackson, and Dr. Sarah Lambart, who offered me a tremendous amount of support and guidance throughout this project. My committee members challenged my abilities as an Earth scientist while steering me through the graduate program and my research project.

I am grateful to my committee member, Dr. Marie Jackson, as well as David S. and Inga M. Chapman for providing me with several opportunities to visit The Advanced Light Source at Lawrence Berkeley National Laboratory. The Advanced Light Source provided invaluable learning opportunities and enabled me to learn from beamline scientists, Dr. Nobumichi Tamura and Dr. Camelia Stan.

I would like to extend my sincere gratitude to my research group (the UPC Fam!) for their help and support throughout this project; and to University of Utah alumnus, Jeremy Fisher, for his work in generating the petrographic thin section scans used for this study. Last but not least, I am deeply indebted to my family and friends who have offered exceptional emotional and financial support during my academic endeavors.

1 INTRODUCTION

Basalt is the most abundant rock type on the surface of Earth and, for nearly 4 billion years, it has interacted with Earth's oceans and atmosphere. Basaltic rock, which is rich in magnetite (Equation 1) and titanomagnetite (Equation 2) is also one of our principal archives for geomagnetic and paleomagnetic studies, and therefore its magnetic properties are a cornerstone of geodynamo and plate tectonic theory.



Both Ti^{4+} substitution (to form titanomagnetite) and low-temperature ($<200^\circ\text{C}$) oxidation (maghemitization) are ubiquitous alteration mechanisms that influence mineral magnetism and the magnetic fidelity of iron oxide minerals in oceanic basalts and basaltic glass (Doubrovine & Tarduno, 2006; Krása et al., 2007; Bowles et al., 2011). During maghemitization, magnetite crystals oxidize as Fe^{2+} diffuses from the crystal interior to a free surface where it is converted to Fe^{3+} (Dunlop & Özdemir, 1997). Partially oxidized magnetite with titanium substitution forms titanomaghemite and is represented by the formula:

$$\text{Fe}_{[2-2x+z(1+x)R]}^{3+} \text{Fe}_{(1-x)(1-z)R}^{2+} \text{Ti}_{xR}^{4+} \square_{3(1-R)} \text{O}_4^{2-} \quad (\text{Equation 3})$$

where $R = 8/[8 + z(1-x)]$, x is the ulvöspinel content and varies from $0 \leq x \leq 1$, z is the oxidation parameter and varies from $0 \leq z \leq 1$, and \square represents a lattice vacancy. The removal of Fe_{2+} from the crystal lattice produces a cation-deficient inverse spinel, such that titanomaghemite has the same crystal structure as titanomagnetite, but the bulk chemical formula of titanohematite. The effect of Fe_{2+} diffusing from the crystal interior to the crystal surface reduces physical grain size on the crystal surface, because the crystal structure of the oxidized maghemite surface layer is smaller than that of the unoxidized magnetite interior. As a result, the oxidized surface stretches and cracks (Figure A1) (Dunlop & Özdemir, 1997). The maghemitization-induced chemical and physical changes to the grain produce crystal lattice vacancies and micrometer-scale conduits for fluids to interact with the reduced magnetite crystal interiors and further accelerate the redistribution of Fe_{2+} (Krása et al., 2005). The removal of Fe_{2+} causes the saturation magnetization of the iron oxides to decrease while the reduction in grain-size generally causes the magnetic coercivity, or hardness, to increase. Thus, maghemitization changes the bulk magnetic properties of a rock *via* chemical alteration and comminution of magnetic domain state.

In basaltic hydrothermal systems, maghemitization of (titano)magnetite crystals proceeds at higher rates through fluid-rock interactions at elevated temperatures (Butler, 1992; Otake et al., 2010; Wang et al., 2020) because maghemitization is fundamentally a thermally-activated diffusion reaction (Dunlop & Özdemir, 1997). Here, we hypothesize that very young oceanic basalt deposits undergo the highest rates of alteration shortly

after eruption, because the reduced rocks are most out of equilibrium with the oxidized seawater environment and the atmosphere. In addition, some of these deposits are at elevated temperature. Maghemitization has the potential to change and even corrupt the magnetization of iron oxides in oceanic crust, thereby limiting our ability to reconstruct Earth's magnetic field with accuracy and precision.

In extreme cases of oxidation, for example when $z > 0.8$, maghemitization can cause self-reversal of the magnetic remanence (Dobrovine & Tarduno, 2004, 2005, 2006; Krása et al., 2005; Coe et al., 2014). Self-reversal describes a remanent magnetization that is antiparallel to the Earth's magnetic field at the time the magnetization is acquired. Because maghemitization of oceanic basalt is ubiquitous, its effects on the magnetic recording fidelity of magnetic materials should be carefully considered. Thus, accurately quantifying the degree of oxidation, or the z parameter, is important for ensuring the reliability of paleogeographic reconstructions, such as testing the paleolatitude stability of oceanic hotspots (McElinny & McFadden, 2000; Tarduno et al., 2003; Dobrovine & Tarduno, 2004, 2005, 2006).

The rates at which maghemitization and Ti^{4+} substitution can proceed over just a few decades in young oceanic basalts is poorly understood. In this study, we investigate basaltic lapilli tuff from drill cores acquired in 2017 through the subaerial, submarine, and sub-seafloor deposits at Surtsey volcano, Iceland (Jackson et al., 2019a). Surtsey is a small submarine to emergent volcano that erupted from 1963 to 1967 in the southern offshore extension of the southeastern Icelandic Rift zone (Thórarinnsson et al., 1964; Thórarinnsson, 1967). Time-lapse cored boreholes acquired in 1979 and 2017 traverse its subaerial, submarine, and sub-seafloor basaltic deposits (Jakobsson & Moore, 1982,

1986; Jackson et al., 2019b; Weisenberger et al., 2019; Moore & Jackson, 2020). The freshly erupted tephra consolidated to form lapilli tuff in the sub-surface deposits through fluid-rock interactions with meteoric water, seawater, and hydrothermal fluids of evolving composition in the diverse fluid and temperature environments of the volcano (Jakobsson & Moore, 1982, 1986; Jackson et al., 2019b; Jackson, 2020; Prause et al., 2020). The chemical and physical alteration of the tephra and lapilli tuff through palagonitization processes also potentially exposed iron oxides to diverse alteration processes that may thereby accelerate changes to the original magnetic remanence carrying minerals. Initial investigations of the 1979 Surtsey core suggested that the dominant magnetic remanence carriers in Surtsey deposits are titanomagnetite (Equation 2) and titanomaghemite (Equation 3) (Grommé, 1982). The comprehensive monitoring of Surtsey since the 1963-1967 eruptions and the record of time-lapse cored boreholes through the still hot deposits provide an ideal environment to study the natural tempo of maghemitization and Ti^{4+} substitution through fluid-rock interactions in emergent and marine basaltic systems. In particular, we ask: can rapid maghemitization and Ti^{4+} substitution progress and thereby change the magnetic properties of the primary magnetic remanence-carrying iron oxides during this decadal-scale time window and over a wide-range of temperatures and fluid compositions? If so, then what are the characteristics and pervasiveness of alteration, and in which hydrothermal conditions is the magnetic alteration most pronounced?

To address these questions, we investigate changes in the chemical and physical properties of the principal magnetic remanence carrying minerals in drill core samples through the Surtsey deposits. The drill cores were acquired through the International

Continental Scientific Drilling Program Expedition 5059, the Surtsey Underwater volcanic System for Thermophiles, Alteration processes and INnovative Concretes (SUSTAIN) project (<https://surtsey.icdp-online.org>), which undertook drilling operations on Surtsey during the summer of 2017 (Jackson et al., 2019a; Weisenberger et al., 2019). We use a suite of rock magnetic studies to identify features that are diagnostic of maghemitization. We provide rock magnetic analyses using thermomagnetic experiments, first-order reversal curve (FORC) diagrams, bulk magnetic remanence and coercivity measurements, and magnetic susceptibility measurements. We also isolate paleomagnetic directions from the basaltic tuff using alternating field (AF) demagnetization. We situate these results in the context of initial material properties measurements and petrographic studies of thin section scans of the tuff samples to further describe the alteration fabrics in these rocks. With this information, we characterize the mineral composition and magnetic domain state of the principal magnetic remanence carriers. We also estimate the oxidation parameter and extent of Ti^{4+} substitution, commonly referred to as the ‘z’ and ‘x’ parameters, respectively (O’Reilly, 1984), during the first 50 years after eruptions terminated at Surtsey in 1967. The results of these investigations provide foundational insights into potential alteration rates of iron oxide minerals in subaerial and marine basaltic systems worldwide.

2 GEOLOGIC SETTING

Surtsey is an isolated oceanic island produced by explosive and effusive eruptions in 1963-1967, 32 km from the south coast of Iceland in the Vestmannaeyjar archipelago. The island marks the offshore, southward-propagating tip of Iceland's South Eastern Rift Zone (Figure 1a) (Einarsson, 2008; Jakobsson et al., 2009). Eruptive activity first emerged at the ocean surface in 1963 and terminated in 1967 (Thórarinnsson et al., 1964; Thórarinnsson, 1967, 1969). Early stage phreatomagmatic eruptions were followed by mid- to late-stage effusive eruptions (Thórarinnsson et al., 1964; Thórarinnsson, 1967; Jakobsson & Moore, 1982). The island emerged from a seafloor depth of about 130 m below sea level (Thórarinnsson et al., 1964; Thors & Jakobsson, 1982; Jakobsson et al., 2009) and the Surtur and Surtungur tuff cones attained a final height of 150 m above sea level (Figure 2). The Surtsey explosive eruptions occurred as a complex sequence of intermittent tephra-finger jets and continuous uprush explosive eruptions (Thórarinnsson et al., 1964; Thórarinnsson, 1965; Jakobsson & Moore, 1982; Moore, 1985). This explosive phase was followed by effusive lava flows that produced a total of ~1 km³ of eruptive products when volcanic activity ceased in June 1967 (Thórarinnsson, 1967, 1969). The dominant lithology at Surtsey is basaltic lapilli tuff (Figure 3a) of rather uniform composition (Schipper et al., 2015, 2016).

Two drilling projects have explored subsurface processes at Surtsey (Jakobsson & Moore, 1982, 1986; Jackson et al., 2019a; Weisenberger et al., 2019). In 1979 a cored

borehole, SE-01, reached 181 meters below the surface (m.b.s.). Initial investigations of the 1979 SE-01 core (Figure 2) described volcanic structures both above and below sea level, the thermal system, and the composition and alteration of basaltic tephra (Jakobsson & Moore, 1982, 1986). In 2017, the SUSTAIN project drilled three cored boreholes through the basaltic tuff, tephra, and minor intrusions of the volcano. The three wellheads – SE-02a, SE-02b, and SE-03 – lie within a 10 m wide area on the ground surface of unconsolidated tephra on the southern flank of the Surtsey tuff cone (Figure 1). For the purpose of this study, we focus on cores SE-02b and SE-03. The vertical borehole, SE-02b, parallels the 1979 SE-01 borehole and extends to 191.64 m.b.s. with 97% overall core recovery (Figures 2 and 3a). Borehole SE-03 is inclined 35° from vertical toward an azimuth of 264° and achieved a final inclined length of 354.05 m measured depth (Figures 2 and 3a). Core SE-03 traverses the sub-seafloor lapilli tuff deposits and the deep vent structure and basaltic intrusions to a total vertical depth of 290 m.b.s. and a horizontal distance approximately 203 m west of the wellhead. Core recovery was nearly 100% through the lapilli tuff but varied from 40 to 90% in basaltic intrusions (Figure 3a) (Jackson et al., 2019a).

The heat anomaly measured at about 100 m b.s. in the 1979 SE-01 borehole was thought to have been produced by nearby dikes that fed effusive lavas between 1966 and 1967 (Figure 3b) (Jakobsson & Moore, 1986). However, the paucity of intrusive basalt encountered by the 2017 SUSTAIN drilling project challenges this hypothesis (Moore & Jackson, 2020) and alternative heat sources must be considered, including the 80-m-thick lava shield that occupies Surtur crater (Figure 2).

Various structural and alteration zones have been identified in the subaerial to submarine to sub-seafloor deposits (Jakobsson & Moore, 1986; McPhie et al., 2020; Prause et al., 2020; Jackson, 2020). In this paper, we distinguish seven alteration zones to investigate the extent of iron oxide mineral alteration in the basaltic lapilli tuff deposits.

These are modified from Jackson (2020):

- (1) subaerial tuff cone (0 – 58 m.b.s.),
- (2) tidal flux zone (58 – 65 m.b.s.),
- (3) upper submarine tuff deposits (65 – 145 m.b.s.),
- (4) submarine inflow zone where cooler water of high salinity enters the borehole (145 – 155 m.b.s.) (Jackson et al., 2019a),
- (5) lower borehole tuff deposits (155 – 185 m.b.s.),
- (6) upper sub-seafloor tuff deposits (185 – 205 m.b.s.),
- (7) lower sub-seafloor tuff deposits (272 – 285 m.b.s.) (Figures 2 and 3d).

The depths do not necessarily indicate where the characteristics of the sample first formed, given the postulated diatreme-like structure below the Surtur vent (Figure 2) (Moore, 1985; Jackson et al., 2019a; Moore & Jackson, 2020). We direct the reader to Jakobsson and Moore (1986) and Jackson et al. (2019a) for a more detailed description of temperature variations in the hydrothermal system.

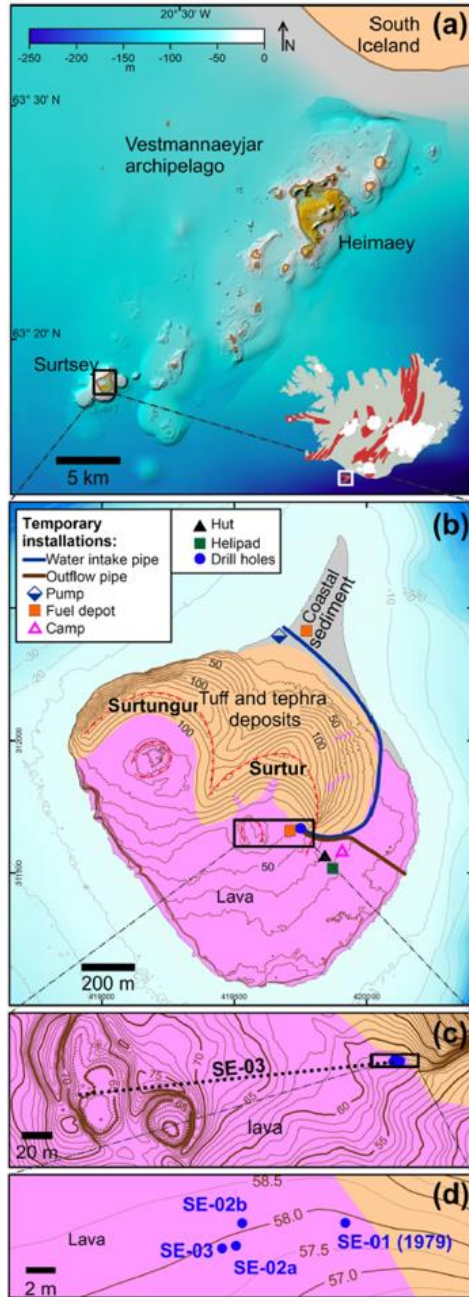


Figure 1: Maps showing drilling operations at Surtsey volcano, Iceland. **(a)** The Vestmannaeyjar volcanic archipelago at the southern offshore extension of the eastern Iceland rift zone (bathymetry: Icelandic Coast Guard, Hydrographic Department). The red elongated patches on the Iceland map illustrate rifts. **(b)** A simplified geologic map of Surtsey (following Jakobsson, 2000) and temporary installations of the 2017 SUSTAIN drilling operation. The red dashed lines indicate crater rims. **(c)** Horizontal projection of the SE-03 (5059-1-D) cored borehole. **(d)** Wellhead locations: SE-01 (1979) and SE-02b, and SE-03 (or 5059-1-B, 5059-1-C, and 5059-1-D) (2017) (from Jackson et al., 2019a).

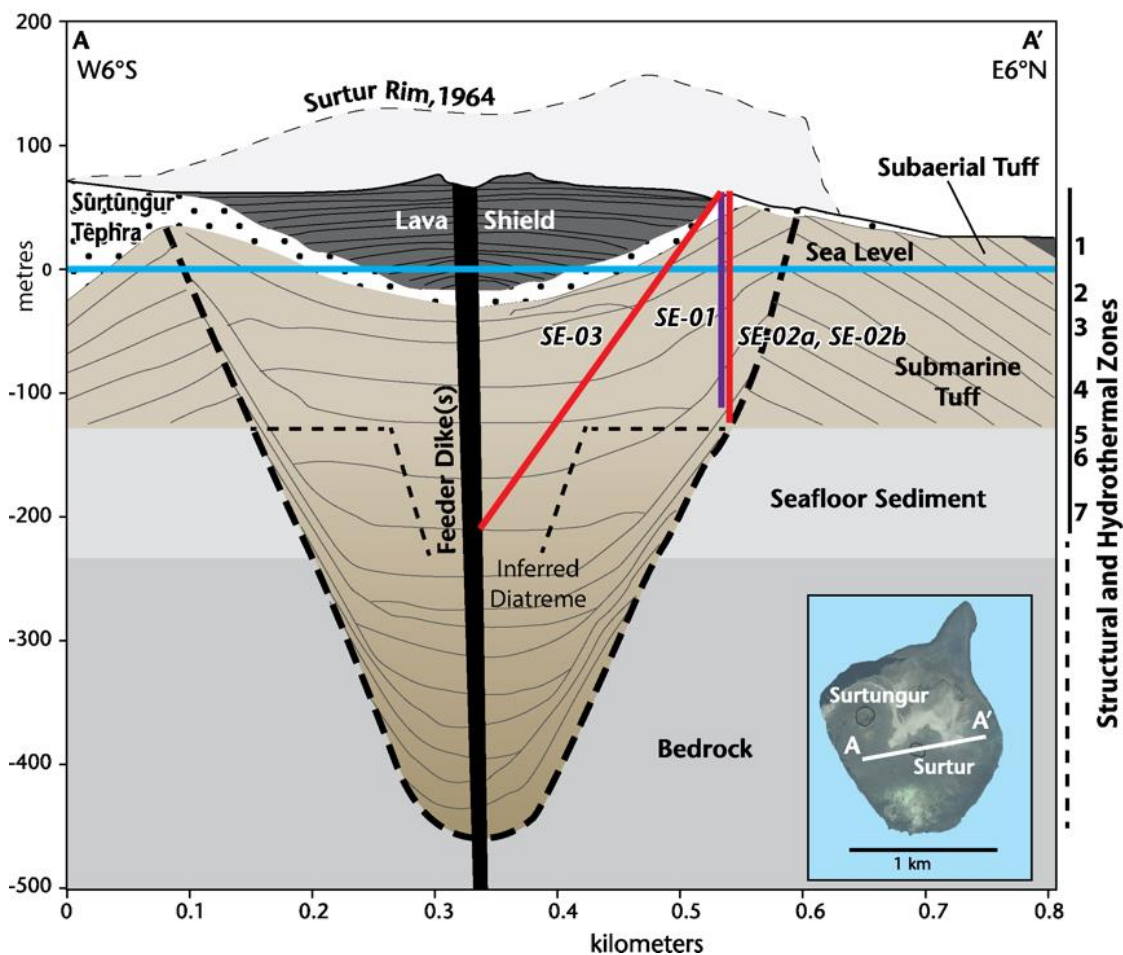


Figure 2: Interpretive, diagrammatic cross-section of Surtsey showing eruptive deposits, seafloor sediments and sedimentary rocks, and a lava shield in the central crater (modified after Moore, 1985; Jakobsson et al., 2009; Jackson et al., 2019a; Jackson, 2020). The bold dashed line shows the sub-seafloor diatreme inferred by Moore (1985). The light dashed line shows the minimum subsurface vent and conduit deposits that will fit 2017 drilling results (Jackson et al., 2019a). Locations of the seven distinct structural and hydrothermal zones shown to the right: (1) subaerial tuff cone (0 – 58 m.b.s.), (2) tidal flux zone (58 – 65 m.b.s.), (3) upper submarine tuff deposits (65 – 145 m.b.s.), (4) submarine inflow zone (145 – 155 m.b.s.), (5) lower borehole tuff deposits (155 – 185 m.b.s.), (6) upper sub-seafloor tuff deposits (185 – 205 m.b.s.), (7) lower sub-seafloor tuff deposits (272 – 285 m.b.s.).

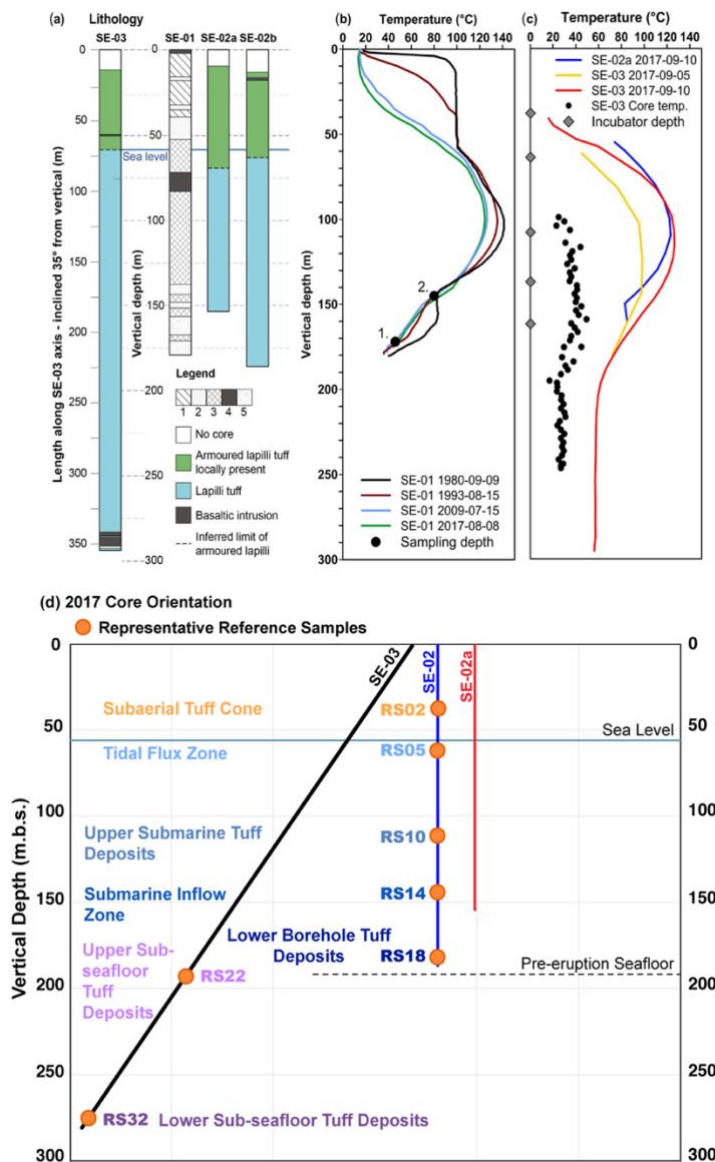


Figure 3: Comparisons of the 1979 and 2017 cored Surtsey boreholes. **(a)** Lithological logs of the 1979 core: SE-01 (following Jakobsson & Moore, 1982). (1) Weakly altered hyaloclastite, brown-black; (2) coarse and poorly graded hyaloclastite, black; (3) sound hyaloclastite, greyish-green; (4) basaltic intrusions and lava (at top), black; and (5) incoherent tephra. Lithological logs of the 2017 simplified core logs: SE-02a, SE-02b, and SE-03 (following Weisenberger et al., 2019). **(b)** Borehole temperatures: SE-01 with 1980, 1993, 2009, and 2017 measurements, as well as 2009 microbiological samples (1, 2) (Jakobsson & Moore, 1982; Jakobsson et al., 2000; Marteinsson et al., 2015). **(c)** Borehole temperatures measured shortly after termination of drilling in SE-02b and SE-03 as well as depths of incubation experiments in SE-02b. **(d)** Cross section of cored boreholes SE-02a, SE-02b, and SE-03 showing the locations in meters below the surface (m.b.s.) of the seven representative reference samples with their respective alteration zones. Figure modified from Jackson et al. (2019a).

3 MATERIALS AND METHODS

3.1 Core Material and Reference Samples

Freshly erupted Surtsey tephra was composed of glass, crystals, and occasional lithic fragments derived from seafloor sedimentary rocks (Lorenz, 1974; Jakobsson & Moore, 1982). The lithified tephra, mainly lapilli tuff, is composed of altered glass, crystals, occasional lithic fragments and authigenic mineral cements; rare traces of fresh glass remain in some pyroclasts (Jakobsson & Moore, 1982, 1986; Jackson et al., 2019b; Prause et al., 2020). Lithic fragments of seafloor rocks and exotic clasts in the lapilli tuff are inferred to derive from explosive excavation of the seafloor by continuous uprush eruptions underlying the Surtur and Surtungur craters (Figure 1b) (Alexandersson, 1970, 1972; Moore, 1985; Baldursson & Ingadóttir, 2007; Reynisson & Jakobsson, 2009; Jackson, 2020). The submarine and sub-seafloor lapilli tuff include porous tuff deposits that have a variety of fine ash rims on altered glass pyroclasts (Moore & Jackson, 2020; Jackson, 2020). Borehole temperatures recorded in 1980 revealed an active hydrothermal system in which basaltic tuff and tephra attained temperatures as high as 141 °C at 100 m.b.s. Temperatures in the 1979 SE-01 borehole have been monitored since 1980 (Jakobsson et al., 2000; Marteinsson et al., 2015; Jackson et al., 2019a). These record differential cooling rates in the deposits from 1980 to 2017.

Thirty-three reference samples were collected from 2017 cores SE-02b and SE-03 and then distributed among the SUSTAIN science team members for collaborative,

interdisciplinary investigations (Jackson et al., 2019a). For this study, we sub-sampled the thirty-two reference samples from the short sections of the working halves of cores SE-02b and SE-03 for initial investigations of the basaltic tuff. Informed by petrographic and material properties investigations (Jackson et al., 2019a; Jackson, 2020), we then identified seven alteration zones and selected a sub-set of seven ‘representative’ reference samples for more detailed investigations. These seven samples occur in the subaerial tuff cone, tidal flux zone, upper submarine tuff deposits, submarine inflow zone, upper sub-seafloor tuff deposits, and lower-sub-seafloor tuff deposits (Figure 3d). From 1980 to 2017, temperatures in the 1979 SE-01 borehole through the subaerial tuff cone at 0 – 58 m.b.s. decreased from ~100 to 70 °C (Figures 3b). In the tidal flux zone, there was a slight decrease in temperature from ~100 to 90 °C. The borehole temperatures through the upper submarine tuff deposits reached 141 °C at 100 m.b.s. in 1980 and decreased to 124 °C during the intervening 38 years. Borehole temperatures remained at about 80 °C in the submarine inflow zone and have decreased to about 50 °C near the bottom of the lower borehole tuff deposits (Figures 3b, c). Temperatures of water samples collected in 2018 from the SE-03 borehole give temperatures of 81 °C at 197 m.b.s. in the upper sub-seafloor tuff deposits and 57 °C at 272 m.b.s. in the lower sub-seafloor tuff deposits (Kleine et al., in press).

3.2 Petrographic Observations

We performed thin section scans in plane polarized and cross polarized light using a Zeiss M2 Petrographic Microscope and an Axiocam Camera, with images stitched together using the Zen 2 pro software in the Marine Paleoecology Imaging Laboratory at

the Department of Geology and Geophysics, University of Utah. The scans produced a 600-700 MB high resolution digital image of the entire thin section from which smaller areas could be studied at high magnification. Munsell colors were determined with the Geological Society of America Rock-Color Chart (<https://munsell.com/munsell-rock-color-chart>).

3.3 Rock Magnetic Measurements

Rock-magnetic experiments were completed at the Utah Paleomagnetic Center, Department of Geology and Geophysics, University of Utah. Reference samples used for magnetic measurements were cut from short sections of the working halves of Cores SE-02b and SE-03 in the Rock Preparation Laboratory at the University of Utah, Salt Lake City, Utah, USA. We prepared ~7 cm³ cubes using a dry saw and stored the samples in a refrigerator at ~4 °C after preparation to minimize laboratory-induced alteration.

3.4 Weak-Field Magnetic Measurements

We measured low-frequency bulk magnetic susceptibility (χ_{lf}) to estimate the concentration of magnetic material within each specimen. Measurements were performed at room-temperature on the cubed specimens. We used an AGICO MFK1 kappabridge with an applied field of 200 A/m at a frequency of 976 Hz. We also measured the high-frequency magnetic susceptibility (χ_{hf}) of each sample in an applied field of 200 A/m at 15,616 Hz. We calculated frequency-dependent magnetic susceptibility (χ_{fd}), which is a parameter sensitive to the absolute concentration of the superparamagnetic particles in

the bulk sample. The χ_{fd} parameter is defined by Dearing et al. (1996), Liu et al. (2004), and Hrouda (2011) as:

$$\chi_{fd} = 100(\chi_{lf} - \chi_{hf})/\chi_{lf} \text{ (\%)} \quad \text{(Equation 4)}$$

To compare the χ_{fd} parameter measured by the Kappabridge to the values measured using a Bartington susceptibility meter, we adjusted the MFK1-measured χ_{fd} parameter using the following equation (Table A1) (Hrouda, 2011):

$$X_{fb} = \frac{\ln 10}{\ln(f_{hf}) - \ln(f_{lf})} X_{fd} \quad \text{(Equation 5)}$$

In the Bartington instrument $\chi_{fb} = \chi_{fd}$; in other instruments the χ_{fb} parameter will differ according to the frequencies used.

Temperature dependence of magnetic susceptibility ($\kappa(T)$) is widely used to assess the composition of magnetic mineralogy (Özdemir, 1987; Liu et al., 2004; Dubrovine & Tarduno, 2004). We performed $\kappa(T)$ measurements on powdered samples (<0.5 g of material crushed to a fine sand size) using an AGICO MFK1 multifunction kappabridge. We performed these measurements in consecutive heating-cooling cycles (*i.e.*, progressive $\kappa(T)$ curves) in air with sequentially increasing maximum temperatures (200, 250, 300, 400, 500, 600, and 700 °C) at 11.8 °C/min following Dubrovine and Tarduno (2006) and Coe et al. (2014). We use these data principally as a proxy for Curie temperature and to recognize the temperature of magnetic mineral transformation. We

also measured a continuous heating-cooling $\kappa(T)$ curve for each sample in an argon atmosphere up to 700 °C at 42.5 °C/min. This experiment follows Özdemir (1987) and Dubrovine and Tarduno (2006) and was designed to help observe and test the temperature at which magnetic mineral alteration first begins in a single thermomagnetic run. The higher treatment rate was chosen to minimize experimentally-induced alteration during heating.

3.5 High-Field Magnetic Measurements

We measured the natural remanent magnetization (NRM) of each sample using an AGICO JR-6A automated spinner magnetometer. Following measurement of NRM, we stepwise demagnetized each specimen using alternating field (AF) cleaning. Each specimen was demagnetized along its three principal axes using a Magnon AFD300 alternating field demagnetizer (typically) to a maximum field of 260 mT. Measurements were performed on the same cubed specimens used for the room-temperature magnetic susceptibility experiments. With each demagnetization step, we alternated the axis along which each specimen was demagnetized (from +x, +y, +z to -x, -y, -z) to minimize possible effects of a gyroremanent magnetization (*e.g.*, Finn et al., 2016).

We plotted these data on orthogonal vector plots to assess directionality and stability using the Pmag GUI 4.2.17 from the PmagPy software (Tauxe et al., 2016). We used the following criteria for calculating the characteristic remanent magnetization (ChRM) directions: (1) at least four successive demagnetization steps define the ChRM; (2) demagnetization trajectories of the ChRM point toward, but do not include, the origin of the orthogonal vector plots; and (3) the maximum angular deviation of the ChRM data

should not exceed 15°. Reference samples from both Cores SE-02b and SE-03 were azimuthally unoriented. We calculated the mean ChRM inclination in Core SE-02b using the Arason-Levi inclination-only method (Arason & Levi, 2010). We also calculated the median destructive fields for each specimen from these demagnetization data.

We measured the anhysteretic remanent magnetization (ARM) to estimate the relative abundance of single domain material in each specimen (Dunlop & Özdemir, 1997; Egli & Lowrie, 2002). Prior to measuring the ARM, each AF-demagnetized specimen was demagnetized again along its three principal axes in a 260 mT field. Each specimen was then placed in a 100 mT alternating-current field with an applied direct-current field (H_0) of 1.0 μ T along the z-axis of the specimen. After imparting an ARM, we measured the remanent magnetization intensity (M_{ARM}). We calculated the susceptibility of anhysteretic remanent magnetization (χ_{ARM}) using the following equation (after Dunlop & Özdemir, 1997):

$$\chi_{ARM} = M_{ARM}/H_0 \quad \text{(Equation 6)}$$

The χ_{ARM} values were then normalized to that of the specimen with the lowest χ_{ARM} intensity to accentuate stratigraphic variations in this parameter. All measurements were completed using an AGICO JR-6A automated spinner magnetometer and a Magnon AFD300 alternating field demagnetizer.

Bulk rock magnetic hysteresis parameters (saturation remanent magnetization (M_{rs}), saturation magnetization (M_s), and coercivity (B_c)) were measured to characterize the bulk rock magnetic stratigraphy of the sampling interval. We performed standard

magnetic hysteresis experiments on all specimens at room temperature using a Lakeshore Cryotronics/PMC Model 3900-4 vibrating sample magnetometer. Raw magnetic hysteresis data were uploaded to the Institute for Rock Magnetism Data Base (IRMDB) from which hysteresis parameters were calculated (Jackson & Solheid, 2010). Hysteresis loops were measured using a maximum applied field of 1.4 T, a field increment 2.5 mT, and an averaging time 100 msec. The approximate mass of representative sample chips for these measurements was ~0.1 g; exact values are provided in Table A1.

We used two additional parameters calculated from the IRMDB: the S-ratio and sigma hysteresis. The S-ratio quantifies relative abundance variations of ferrimagnetic and antiferromagnetic minerals in bulk specimens. S100, or the magnetic ‘softness’ ratio, reveals the relative abundance of low-coercivity magnetic minerals in each specimen. As S100 approaches unity, low-coercivity minerals such as magnetite and maghemite are interpreted to magnetically dominate samples. In contrast, when S100 approaches zero or has negative values, contributions from high-coercivity minerals, such as hematite or goethite, are substantial (Liu et al., 2007). S300, or the magnetic ‘hardness’ ratio, reveals the relative abundance of high-coercivity minerals in bulk specimens. As S300 approaches unity, the relative abundance of high-coercivity magnetic minerals increases. In contrast, a decrease in S300 reflects a greater contribution from low-coercivity magnetic minerals. Sigma hysteresis characterizes the shape of the magnetic hysteresis loop (*e.g.*, square, wasp-waisted, pot-bellied) to reveal the contribution of different grain-size and compositional components to the bulk remanent magnetization. Upright, squarish loops identified by sigma hysteresis values near zero are typically indicative of a homogenous mixture of single domain magnetite grains. A positive sigma hysteresis

corresponds to a ‘wasp-waisted’ hysteresis loop suggestive of mixtures of superparamagnetic and larger magnetic domain states. A negative sigma hysteresis corresponds to a ‘pot-bellied’ hysteresis loop, typically characteristic of combinations of magnetically hard and soft magnetic components (Tauxe et al., 1996; Fabian, 2003).

We measured direct-current demagnetization curves to calculate the coercivity of remanence (B_{cr}). All direct-current demagnetization curves were measured using the same instrument used for the bulk rock magnetic hysteresis measurements. We used the following measurement parameters: 0 mT starting field, 1.5 T saturating field, a total of 150 points/curve using a logarithmically increasing field increment, and a two-second averaging time.

We measured first-order reversal curve (FORC) diagrams to diagnose the magnetic domain state of each of the seven representative reference samples. FORC diagrams represent magnetic coercivity and magnetic interaction field distributions along the horizontal and vertical axes, respectively (Egli, 2013; Roberts et al., 2014). A FORC diagram is calculated from a series of partial magnetic hysteresis loops called first-order reversal curves (Mayergoyz, 1986; Roberts et al., 2014). A FORC is measured by first exposing a sample to a strong positive applied magnetic field, where the sample (typically) reaches magnetic saturation. The applied magnetic field is subsequently decreased to a reversal field, and to produce a FORC diagram, multiple FORCs are measured over a range of uniformly spaced reversal fields. The FORC distribution is defined as a partial second derivative and is generated from the magnetization data acquired from successive measurement points on successive FORCs (Wilde & Girke, 1959; Mayergoyz, 1986; Pike & Fernandez, 1999; Roberts et al., 2014). We measured

FORCs on the same specimens used for the bulk hysteresis and direct-current demagnetization experiments. We used a 1 T saturating field, 1.06 mT field increment, and a 333 msec averaging time; a total of 240 FORCs were measured for each specimen. FORC data were processed using FORCinel version 3.06 (Harrison & Feinberg, 2008), which implements VARIFORC smoothing (Egli, 2013).

4 RESULTS

4.1 Petrographic and Material Descriptions

Results from our petrographic investigations of thin section scans and material measurements are shown in Figure 4 and Table 1. These reveal differences in: (1) the abundance of weakly-altered glass pyroclasts and the extent of their alteration, (2) the thickness of rinds of palagonitized glass around altered glass pyroclasts, (3) a qualitative estimate of the connected porosity, (4) the overall color of the altered ash matrix of the tuff, and (5) dry density, wet density, and water absorption. In Core SE-02b, for example, specimen RS02, 35 m.b.s., retains occasional weakly-altered glass fragments (A in Figure 4a) with grayish-yellow color Munsell color (5Y 8/4). Palagonitized rinds of variable thickness (90 – 360 μm) (B in Figure 4a) occur along the perimeter of glass pyroclasts with moderate reddish-brown color (10R 4/6). Specimen RS02 appears to have a well-connected porosity, exhibiting abundant large (up to 3.5 mm), irregularly shaped vesicles in the altered vitric matrix. Smaller, spherical vesicles occur within the altered glass pyroclasts. Overall, the tuff matrix is lighter in color (10YR 5/4) than deeper specimens. Specimen RS02 also has the highest water absorption (0.17) of the seven reference samples (Table 1).

Specimen RS05 at 65 m.b.s., shows no visible fresh glass (Figure 4d). This specimen appears to have a well-connected porosity with several large, irregularly shaped vesicles in the altered vitric matrix (Figure 4d). Overall, the tuff matrix is dark gray to

black (N2). In specimen RS10, 111 m.b.s., rare weakly-altered glass pyroclasts (A' in Figure 4e) have grayish-yellow color (5Y 8/4). One such clast has a thick (540 μm) palagonitized rind (B Figure 4e) with moderate reddish-brown color (10R 4/6). Specimen RS10, 111 m.b.s., appears to have a relatively low connected porosity. The altered vitric matrix is highly altered and greenish black (5GY 2/1). Specimens RS14 and RS18, 148 m.b.s. and 181 m.b.s., are unique among the reference sample suite: they contain abundant very weakly-altered glass pyroclasts (A both Figures 4b, c) with a typical grayish-yellow color (5Y 8/4) (Jackson, 2020). In specimen RS14 there are palagonitized glass rinds (10R 4/6) of variable thickness (90 – 360 μm) (B in Figure 4b) around weakly-altered glass pyroclasts (10R 4/6). Specimen RS14 also has the lowest water absorption (0.09) of the seven reference samples (Table 1). In specimen RS18, however, there is a general absence of palagonitized rinds and the glass pyroclasts are very weakly-altered (Figure 4c). Specimen RS18 has the lowest dry density (1.22 g/cm³) and wet density (1.43 g/cm³) of the seven reference samples (Jackson et al., 2019a). Both specimens RS14 and RS18 appear to have a moderately well-connected porosity with fewer large, irregularly shaped vesicles in the altered vitric matrix (Figure 4c). Overall, specimen RS14 exhibits greenish black (5GY 2/1) altered ash matrix, and specimen RS18 exhibits moderate yellow (5Y 7/6) to dusky yellow (5Y 6/4) altered ash matrix.

In Core SE-03, both specimens RS22, 197 m vertical depth, and RS32, 272 m vertical depth, show no visible fresh glass. They contain strongly-altered glass pyroclasts that appear darker in color than those of Core SE-02b (A' in Figures 4f, g). In general, altered glass pyroclasts are moderate yellow (5Y 7/6) to greenish-black (5GY 2/1). Specimen RS22 appears to have the highest connected porosity of the seven reference

samples examined here; there are abundant large, irregularly shaped vesicles in the altered vitric matrix and abundant small, spherical vesicles in strongly-altered glass pyroclasts (Figure 4f). A plagioclase (Pl) crystal fragment remains intact. Specimen RS32 also has the highest dry density (2.05 g/cm³) and wet density (2.33 g/cm³) and appears to have a high connected porosity with a few large, irregularly shaped vesicles in the vitric matrix and abundant small, spherical vesicles in strongly-altered glass pyroclasts. Overall, the altered vitric matrix of both RS22 and RS32 is grayish yellow (5Y 8/4) to dusky green (5G 3/2) (Figures 4f, g).

4.2 Magnetic Susceptibility

Results from bulk magnetic susceptibility measurements of the full suite of 32 reference samples are shown in Figure 5 and Table A1; we have measured and reported a much larger variety of magnetic measurements than presented in Jackson et al. (2019a). Bulk magnetic susceptibility (3rd panel of Figure 5) ranges from 3.8×10^{-7} to 7.8×10^{-7} mass-normalized SI units (m³/kg) in the SE-02b core samples and from 5.7×10^{-7} to 11.9×10^{-7} m³/kg in the SE-03 core samples. In Core SE-02b, the greatest bulk magnetic susceptibility occurs near the upper submarine tuff deposits and the lowest bulk magnetic susceptibility occurs in the tidal flux zone. The greatest changes to bulk magnetic susceptibility occur at and below the upper submarine tuff deposits (between 110 – 128 m.b.s.). The tuff at 180 m vertical depth in inclined Core SE-03 records the greatest bulk magnetic susceptibility; the lowest occurs at 228 m vertical depth. There are two marked increases in bulk magnetic susceptibility in the sub-seafloor tuff deposits: one at 235 m vertical depth and the other at 272 m vertical depth. In general, the tuff samples of Core

SE-03 record greater bulk magnetic susceptibility values than the tuff samples of Core SE-02b.

Results from frequency-dependent magnetic susceptibility are shown in Figure 5 (4th panel) and Table A1. Frequency-dependent magnetic susceptibility ranges from 2.5 to 10.2% and 2.5 to 5.0% in the samples from Core SE-02b and Core SE-03, respectively. The samples of Core SE-02b record the highest values at 165 m.b.s. near the weakly-altered tuff of the submarine inflow zone and the lowest at 101 m.b.s. near the more strongly-altered upper submarine tuff deposits (Figure 5). The greatest changes to frequency-dependent magnetic susceptibility occur at 165 m.b.s. near the submarine inflow zone. The samples from Core SE-03 record the greatest frequency-dependent magnetic susceptibility at 249 m vertical depth and the lowest at 180 m vertical depth (Figure 5). In general, the tuff samples of Core SE-02b record greater variation in frequency-dependent magnetic susceptibility than the tuff samples of Core SE-03.

Continuous heating-cooling $\kappa(T)$ curves for the seven representative reference samples are shown in Figure 6. These measurements show inferred Curie temperatures of the original magnetic phases between 300 – 450 °C for five specimens (Figures 6a, d-g); specimens RS14 and RS18 are exceptions. In specimens RS02, RS05, RS10, RS22, and RS32, an immediate increase in magnetic susceptibility occurs upon heating. A broad ‘hump’ occurs in the heating curves between 150 – 350 °C (Figures 6a, d-g). A second hump is also present in the heating curve and occurs around 550 °C (Figures 6b, d-g). This hump near 550 °C is most pronounced in RS14 and RS10. In specimen RS10 (Figure 6e), an additional (third) hump occurs in the heating curve around 460 °C, consistent with observations by Grommé (1982) of a nearby specimen from the 1979

Surtsey core at 107.5 m.b.s. In specimen RS18 (Figure 6c), a slight, steady decrease in magnetic susceptibility occurs with increasing temperature until reaching the inferred Curie temperature of the original magnetic phase near 580 °C. All specimens, with the sole exception of RS32 (Figure 6g), show a final magnetic susceptibility that is higher than the initial magnetic susceptibility measured upon heating.

Results from our progressive $\kappa(T)$ measurements for the seven representative reference samples are shown in Figure 7. The curves begin to exhibit irreversibility (*i.e.*, the heating and cooling curves for a single thermomagnetic run are no longer identical) after heating to 250 – 400 °C. This irreversibility becomes more pronounced with each heating step in all progressive heating-cooling cycles, except for specimen RS18 (Figures 7a, b, d-g). A gradual increase in Curie temperature with each heating step first begins at ~400 °C in the original magnetic phase (Figures 7a, d-g). A pronounced increase in magnetic susceptibility begins at temperatures above 200 °C and increases with each heating step to 700 °C. Notably, specimen RS18 is the only sample that exhibits nearly reversible behavior upon heating to ~580 °C (Figure 7c).

4.3 Paleomagnetism

Results from our natural remanent magnetization measurements of the full suite of 32 reference samples are shown in Figure 5 (1st panel) and Table A1. Natural remanent magnetization (NRM) ranges from 0.15 to 2.99 A/m in the SE-02b core samples and 0.80 to 3.22 A/m in the SE-03 core samples. The samples from Core SE-02b record the greatest NRM at 157 m.b.s. near the submarine inflow zone (RS14) and the lowest at 65 m.b.s. in the tidal flux zone (RS05). The greatest change to NRM in the Core SE-02b

samples occurs between 148 – 157 m.b.s. – *i.e.*, in the submarine inflow zone of weakly-consolidated lapilli tuff (Jackson et al., 2019a). The samples from inclined Core SE-03 record the greatest NRM at 235 m.b.s. and the lowest at 228 m.b.s.; the greatest change to NRM is also recorded at this depth interval in the sub-seafloor tuff deposits. In the Core SE-02b samples, the calculated median destructive fields range from 41.4 to 94.1 mT in the tidal flux zone and submarine inflow zone. By contrast, the Core SE-03 samples reveal a relatively uniform distribution in median destructive fields with depth through the sub-seafloor tuff deposits, ranging from 46.6 to 51 mT.

Results from our alternating field demagnetization measurements of SE-02b core reference samples are shown in Table 2 and Figure 8. We identified two components in the demagnetization data: (1) an unstable low-coercivity direction and (2) a stable direction that decays toward the origin of orthogonal vector plots; we assign this second component as the characteristic remanent magnetization (ChRM) direction (Table 2). The low-coercivity component is removed in most samples after 30 mT (*e.g.*, Figure 8b). The majority of samples in Core SE-02b show a well-defined ChRM after 70 mT AF demagnetization treatment (*e.g.*, Figures 8b, c).

We calculated a maximum likelihood estimate of magnetic inclination of 77° with an estimated Fisher precision parameter (k) of 450 and a 95% confidence limit (a_{95}) of 2° ($n = 12$) (following the method of Arason and Levi (2010)). The mean magnetic inclination of the low-coercivity component is 90° with a $k = 10.3$ and a $a_{95} = \sim 14^\circ$ ($n = 12$).

4.4 High-field Magnetic Remanence

Results from our high-field magnetic remanence measurements of the full suite of 32 reference samples are shown in Figure 5 and Table A1. Susceptibility of anhysteretic remanent magnetization (χ_{ARM}) ranges from 0.003 to 0.070 and 0.011 to 0.095 in the SE-02b and SE-03 core samples, respectively (6th panel of Figure 5). The Core SE-02b samples record the greatest χ_{ARM} at 157 m.b.s. near the submarine inflow zone (RS14) and the lowest at 101 m.b.s. at the hydrothermal temperature maximum in the upper submarine tuff deposits (RS10). The greatest changes to χ_{ARM} occur from the submarine inflow zone (RS14) to the lower borehole tuff deposits above the pre-eruption seafloor (RS18). The Core SE-03 samples record the greatest χ_{ARM} at 235 m vertical depth (RS27) and the lowest at 229 m vertical depth (RS26). The lapilli tuff of RS26 is highly porous, with water absorption at 19% and dry bulk density of 1.44 g/cm³, while the lapilli tuff of RS 27 is highly compact, with water absorption at 8% and dry bulk density of 2.19 g/cm³ (Jackson et al., 2019a; Jackson, 2020). These specimens reveal the material and magnetic heterogeneities in the sub-seafloor tuff deposits. Similar to NRM, the greatest change to χ_{ARM} occurs between 229 – 235 m vertical depth from the porous to compact tuff fabrics and, again, a marked increase occurs at 180 m vertical depth (RS19) in compact lapilli tuff with abundant mineral cements, with low water absorption, 9%, moderate dry bulk density, 2.08 g/cm³ (Jackson et al., 2019a; Jackson, 2020).

Saturation magnetization (M_s) ranges from 13 to 85 mAm²/kg in the SE-02b core samples and 13 to 381 mAm²/kg in the SE-03 core samples (5th panel of Figure 5, Table A1). The Core SE-02b samples record the greatest M_s near the submarine inflow zone at 157 m.b.s. and the lowest near the tidal flux zone at 56 m.b.s. The Core SE-03 samples

record the greatest M_s at 180 m vertical depth and the lowest at 212 m vertical depth. The greatest change to M_s occurs between the specimen at 180 m vertical depth and that at 235 m vertical depth. The squareness ratio (M_{rs}/M_s) ranges from 0.36 to 0.49 in the samples from Core SE-02b and 0.34 to 0.42 in the samples from Core SE-03 (5th panel). The samples from Core SE-02b record the greatest squareness ratio (0.49) at 157 m.b.s. near the submarine inflow zone and the lowest near maximum hydrothermal temperatures of the upper submarine tuff deposits at 101 m.b.s. The samples from Core SE-03 record the greatest squareness ratio at 180 m vertical depth and the lowest at 229 m vertical depth, again from the more compact (RS19) and more porous (RS26) lapilli tuff deposits. Bulk magnetic coercivity ranges from 21 to 81 mT in the SE-02b samples and 24 to 44 mT in the SE-03 samples. The samples from Core SE-02b record the greatest magnetic coercivity near the submarine inflow zone at 157 m.b.s. and the lowest near the upper submarine tuff deposits at 101 m.b.s., again between lapilli tuff in proximity with the cool pre-eruptive seafloor (RS18) and lapilli tuff at the maximum hydrothermal temperature (RS10). The samples from Core SE-03 record the greatest magnetic coercivity near the lower sub-seafloor tuff deposits at 265 m vertical depth and the lowest at 243 m vertical depth.

The sigma hysteresis ranges from -0.14 to 0.11 in the SE-02b core samples and -0.09 to 0.02 in the SE-03 core samples (8th panel of Figure 5, Table A1). The Core SE-02b samples record the greatest sigma hysteresis near the tidal flux zone at 56 m.b.s. (RS05) and the lowest in the lower borehole tuff deposits at 181 m.b.s. (RS18). The Core SE-03 samples record the greatest sigma hysteresis at 180 m vertical depth and the lowest in the upper sub-seafloor tuff deposits at 197 m vertical depth.

S100, a measure of the relative abundance of magnetically soft minerals, ranges from -0.21 to 0.79 in the Core SE-02b samples and 0.21 to 0.72 in the Core SE-03 samples (9th panel of Figure 5, Table A1). The samples from Core SE-02b record the greatest S100 near the upper submarine tuff deposits at 101 m.b.s. and the lowest near the submarine inflow zone at 157 m.b.s. The samples from Core SE-03 record the greatest S100 at 243 m vertical depth and the lowest near 265 m vertical depth. S300, a measure of the relative abundance of magnetically hard minerals, ranges from 0.82 to 0.99 in the Core SE-02b samples and 0.92 to 0.98 in the Core SE-03 samples (9th panel of Figure 5). The Core SE-02b samples record the greatest S300 near the upper submarine tuff deposits at 101 m.b.s. and the lowest near the submarine inflow zone at 157 m.b.s. The Core SE-03 samples record the greatest S300 at 197 m vertical depth and the lowest at 180 m vertical depth.

Results from our FORC measurements of the seven selected reference samples are shown in Figure 9; the smoothing parameters used for the FORC diagrams produced for each specimen are provided in Table A2. All specimens exhibit the following magnetic domain state characteristics: a central ridge and an isolated negative (blue) signal that lies near the y-axis within the $B_u > 0$ region of the FORC diagram. Specimen RS18 (Figure 9c) has the most unique FORC distribution with a peak contribution to the magnetic coercivity distribution near $B_c = 85$ mT and with a peak coercivity that extends to, and presumably exceeds, $B_c = 160$ mT. Specimen RS18 also has a relatively broad and symmetric dispersion around the central ridge. In specimens RS02 (Figure 9a) and RS14 (Figure 9b), there is a shift to lower coercivities with a peak contribution to the magnetic coercivity distribution between $40 < B_c < 45$ mT and contributions from higher

coercivity grains extending to $B_c = 160$ mT. The dispersion of coercivities along the central ridges is broad but it is typically slightly skewed toward lower coercivities (less symmetric) compared to the least altered specimen, RS18. Specimens RS05, RS10, RS22, and RS32 have central ridges with peak contributions to the magnetic coercivity distributions near $B_c = 30$ mT (Figures 9d-g); the negative values of the FORC diagrams vary slightly in magnitude and the shape of their distribution among these specimens; the negative signal is most pronounced in RS32 (Figure 9g).

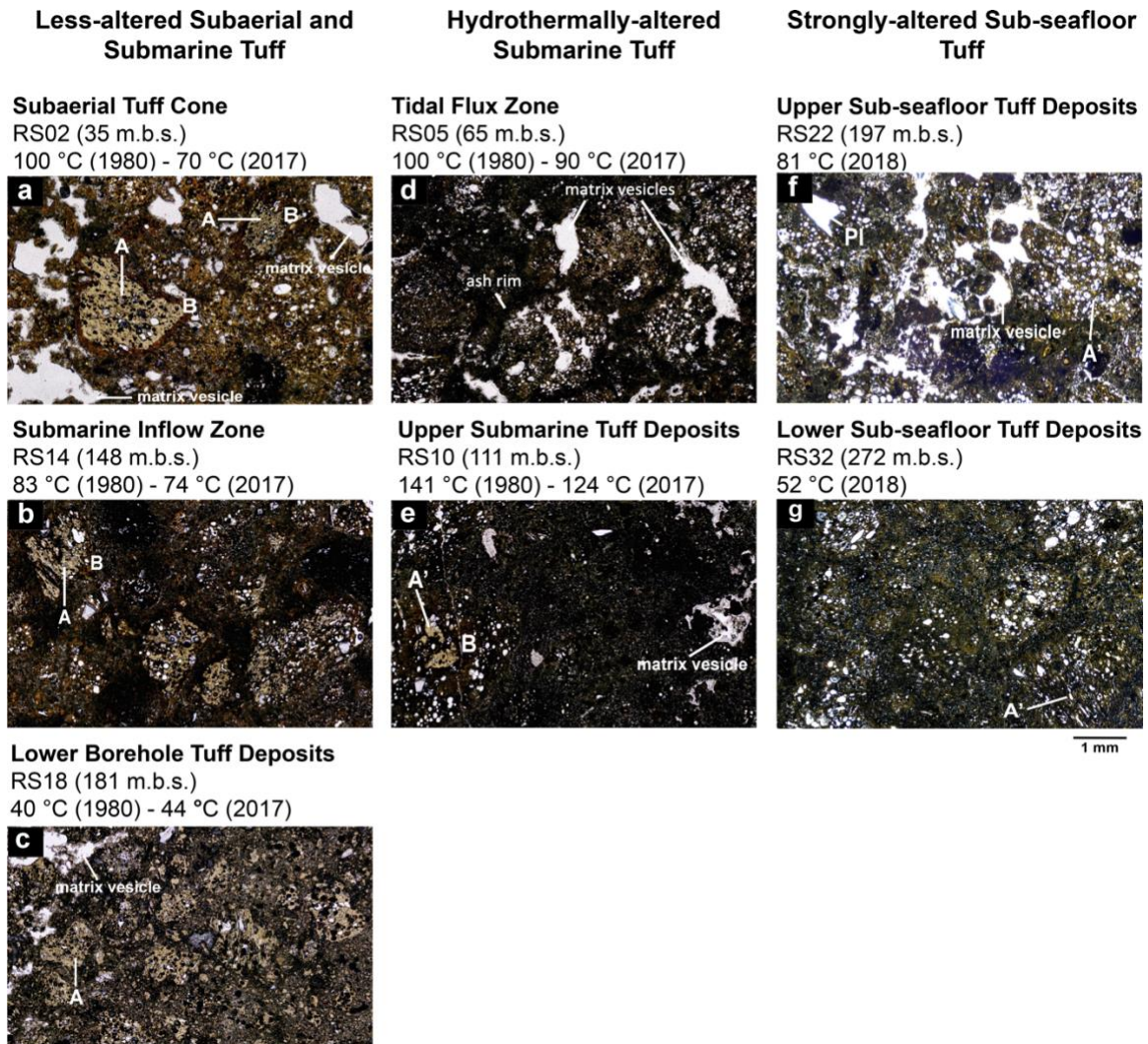


Figure 4: Petrographic thin section scans of the seven representative reference samples from the SE-02b and SE-03 cores. The label A shows the location of very-weakly altered glass pyroclasts; B shows palagonitized rinds around very weakly-altered glass pyroclasts; A' shows strongly-altered glass pyroclasts; and Pl shows a plagioclase crystal. Thin section scans are all shown at the same scale (scalebar shown under Fig. 4g). Temperature estimates from 1980 and 2017 were measured in the SE-01 borehole. The SE-01 borehole temperatures measured in 2017 occurred before the initiation of SUSTAIN drilling of the SE-02b borehole. Temperature estimates from 2018 of Core SE-03 are from Kleine et al. (in press).

Table 1: Dry density, wet density, and water absorption of the seven representative reference samples from 2017 SE-02b and SE-03 cores (from Jackson et al., 2019a). Measurements follow ASTM C97-18, with volume computed from half- or whole-round core dimensions.

Reference Number	Specimen ID	Dry Density (g/cm ³)	Wet Density (g/cm ³)	Water Absorption	Petrographic Observations
SE-02B					
RS-2	5059-1-C-9-2, 58-88	1.54	1.86	0.17	Several very weakly-altered glass pyroclasts (5Y 8/4)* with palagonitized glass rinds (10R 4/6) of variable thickness (90-360 µm). Well-connected porosity with abundant large, irregularly shaped vesicles in the altered matrix. Small, circular vesicles are abundant in weakly-altered glass pyroclasts. Overall, tuff matrix is lighter in color (10YR 5/4) than deeper specimens.
RS-5	5059-1-C-22-2, 57-87	1.67	1.94	0.14	No visible fresh glass present. High connected porosity with several large, irregularly shaped vesicles in the altered ash matrix. Abundant small, circular vesicles in altered glass pyroclasts. Overall, the matrix is dark gray to black (N2).
RS-10	5059-1-C-39-2, 68-98	1.88	2.14	0.12	Rare strongly-altered glass pyroclasts (5Y 8/4) with thick (540 µm) palagonitized rinds (10R 4/6). Relatively low connected porosity. Overall, the matrix is greenish black (5GY 2/1).
RS-14	5059-1-C-52-3, 60-89	1.94	2.13	0.09	Abundant very weakly-altered glass pyroclasts (5Y 8/4) with palagonitized rinds (10R 4/6) of variable thickness (90-360 µm). Moderately well-connected porosity with only a few large, irregularly shaped vesicles in the altered ash matrix and abundant small, circular vesicles in altered glass pyroclasts. Overall, the matrix is greenish black (5GY 2/1).
RS-18	5059-1-C-65-2, 32-64	1.22	1.43	0.14	Abundant very weakly-altered glass pyroclasts (5Y 8/4) with no visible palagonitized rinds and possible fresh glass locally present. Moderately well-connected porosity with only a few large, irregularly shaped vesicles in the matrix and abundant small, circular vesicles in very weakly-altered glass pyroclasts. Overall, the matrix is moderate yellow (5Y 7/6) to dusky yellow (5Y 6/4).
SE-03					
RS-22	5059-1-D-82-4, 58-93	1.53	1.83	0.16	No visible fresh glass present. Glass pyroclasts are strongly-altered (5Y 7/6 to 5GY 2/1). Very high-connected porosity with abundant large, irregularly shaped vesicles in the altered ash matrix and abundant small, spherical vesicles in strongly-altered glass pyroclasts. Overall, tuff matrix is grayish yellow (5Y 8/4) to dusky green (5G 3/2).
RS-32	5059-1-D-112-2, 0-37	2.05	2.33	0.12	No visible fresh glass present. Glass pyroclasts are strongly-altered (5Y 7/6 to 5GY 2/1). High connected porosity with a few large, irregularly shaped vesicles in the altered ash matrix and abundant small, spherical vesicles in strongly-altered glass pyroclasts. Overall, the tuff matrix is grayish yellow (5Y 8/4) to dusky green (5G 3/2).
*Geological Society of America Color Chart					

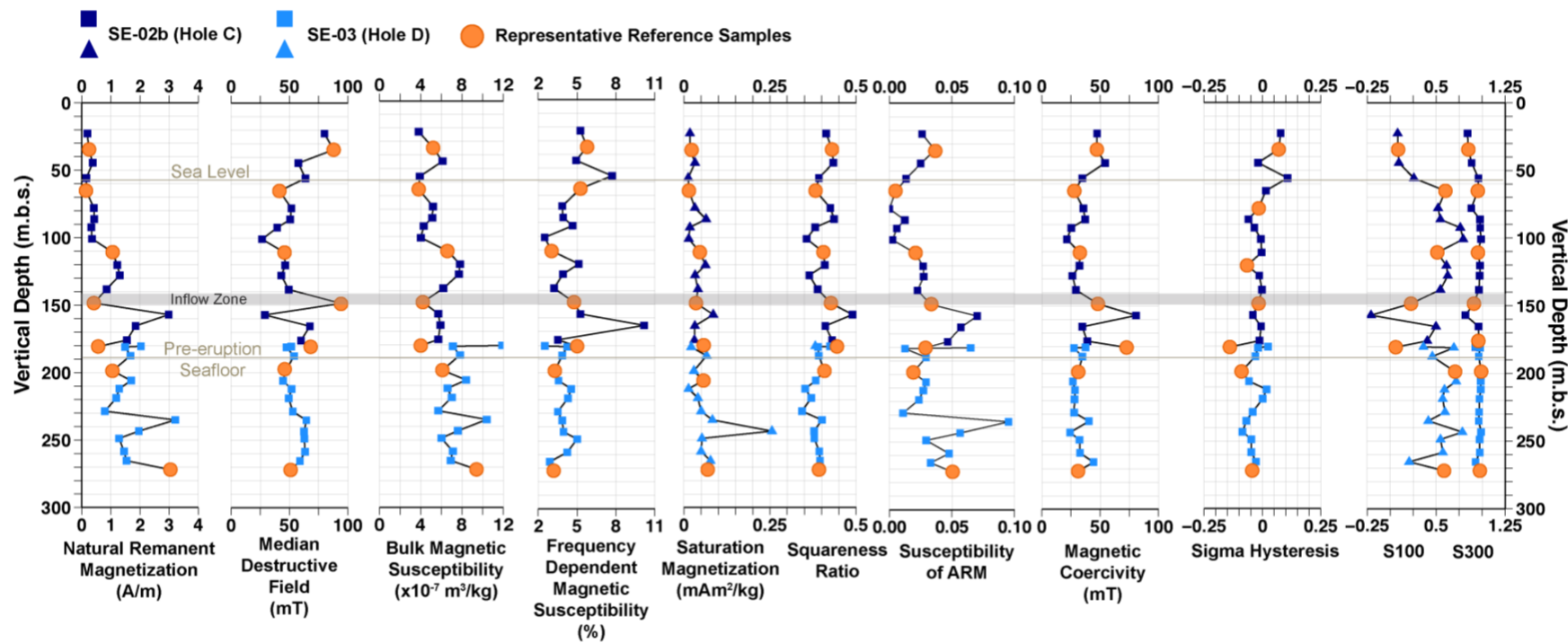


Figure 5: Bulk magnetic properties of the full suite of 32 reference samples (Jackson et al., 2019a). Reference samples from Core SE-02b are shown in dark blue, whereas reference samples from Core SE-03 are shown in light blue. The seven representative reference samples are shown with orange circles. Inflow zone represents the location where cooler water of high salinity enters the borehole. Natural remanent magnetization (1st panel), bulk magnetic susceptibility (3rd panel), and frequency dependent magnetic susceptibility (4th panel) are from Jackson et al. (2019a).

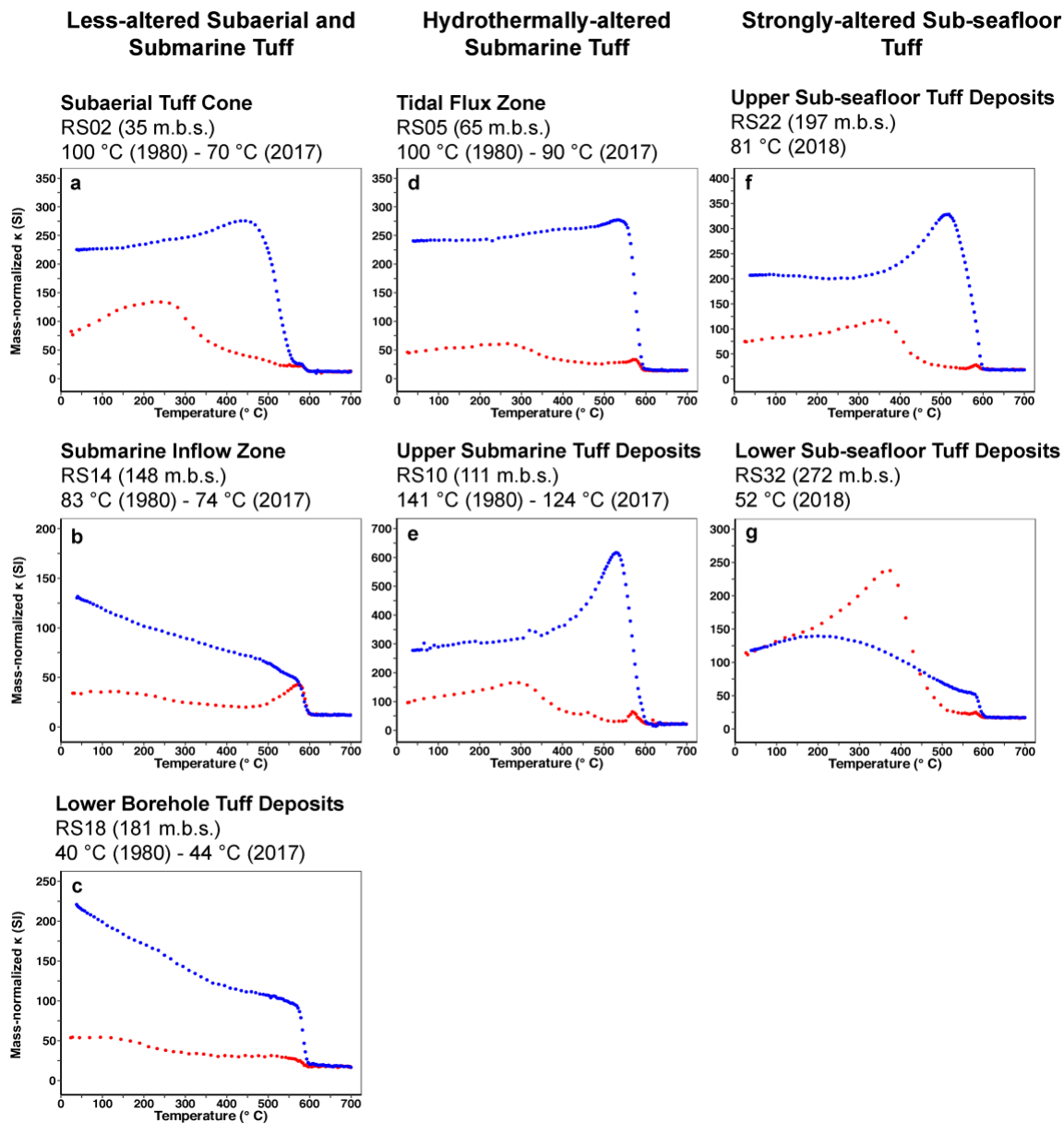


Figure 6: Results from continuous $\kappa(T)$ curves. Mass-normalized magnetic susceptibility measured during a single, continuous heating-cooling $\kappa(T)$ cycle in an argon atmosphere. Heating curves are shown in red and cooling curves are shown in blue.

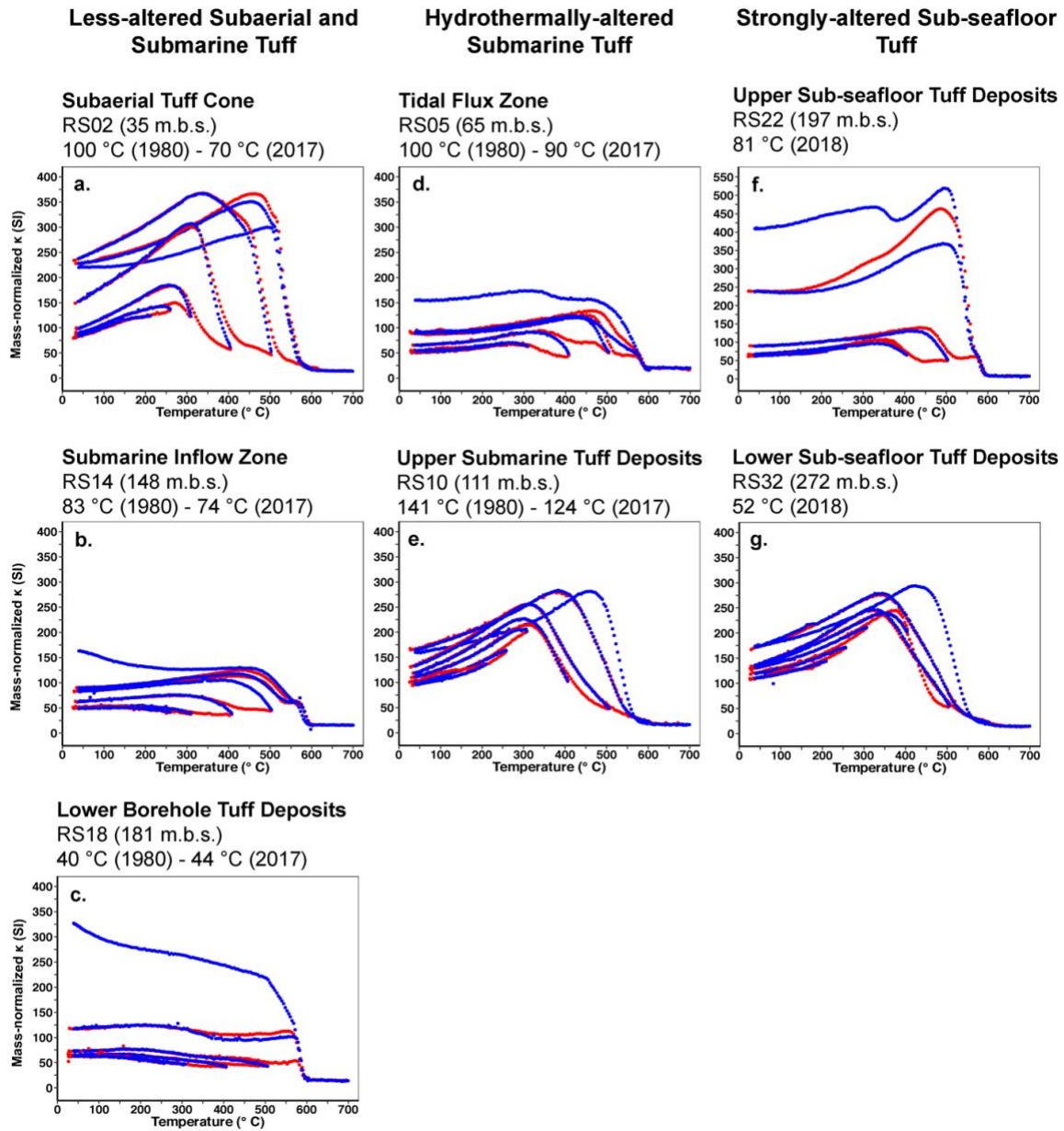


Figure 7: Results from progressive $\kappa(T)$ curves. Mass-normalized magnetic susceptibility measured during a succession of heating-cooling $\kappa(T)$ cycles in an ambient atmosphere. Heating curves are shown in red and cooling curves are shown in blue.

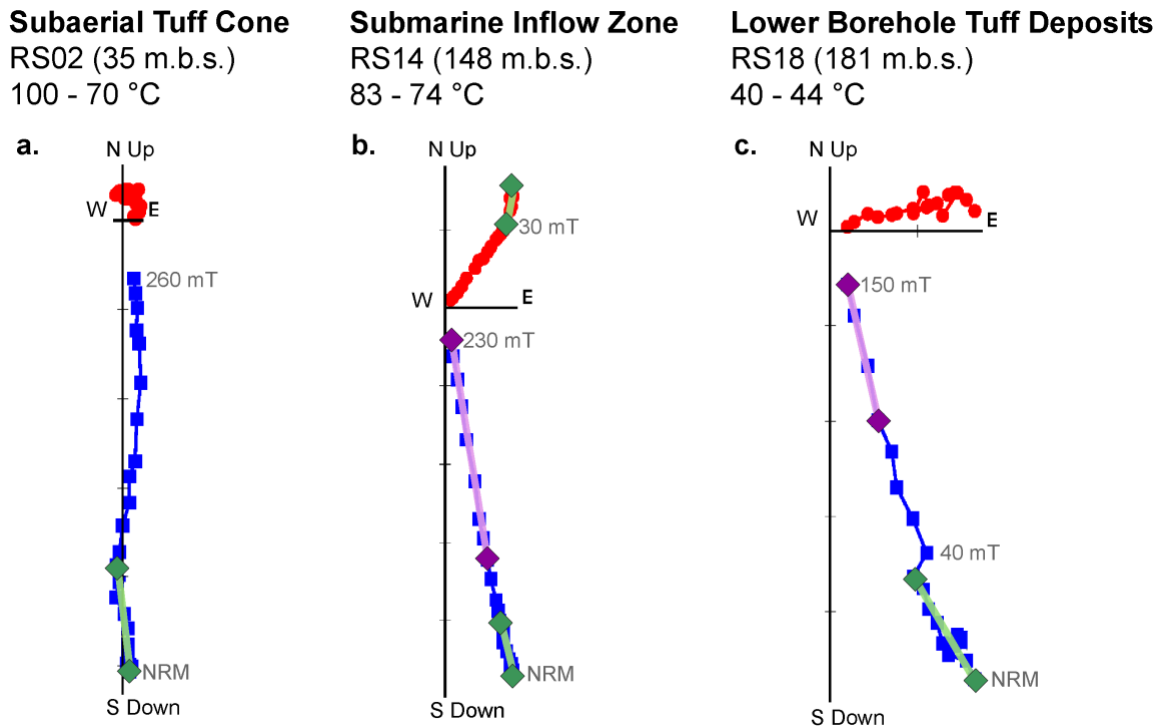


Figure 8: Orthogonal vector plots of demagnetization results from three representative reference samples: RS02, RS14, and RS18. All plots show specimen natural remanent magnetization (NRM) and final demagnetization step. The declinations are shown as red circles and the inclinations are shown as blue squares. Component 1 is shown in green and component 2 is shown in purple. Specimen RS02 shows demagnetization behavior that does not decay to the origin. No characteristic remanent magnetization (ChRM) direction is fit to this and similarly-behaved samples. RS14 shows the most stable demagnetization behavior of the representative reference samples suite. It shows two well-defined components of magnetization marked by an inflection point at 30 mT. Component 1 is from 0 – 30 mT and is interpreted as a drilling induced magnetic overprint. Component 2 is from 60 – 230 mT and shows the interpreted ChRM. RS18 shows typical demagnetization behavior with two directional components to magnetization marked by an inflection point at 40 mT.

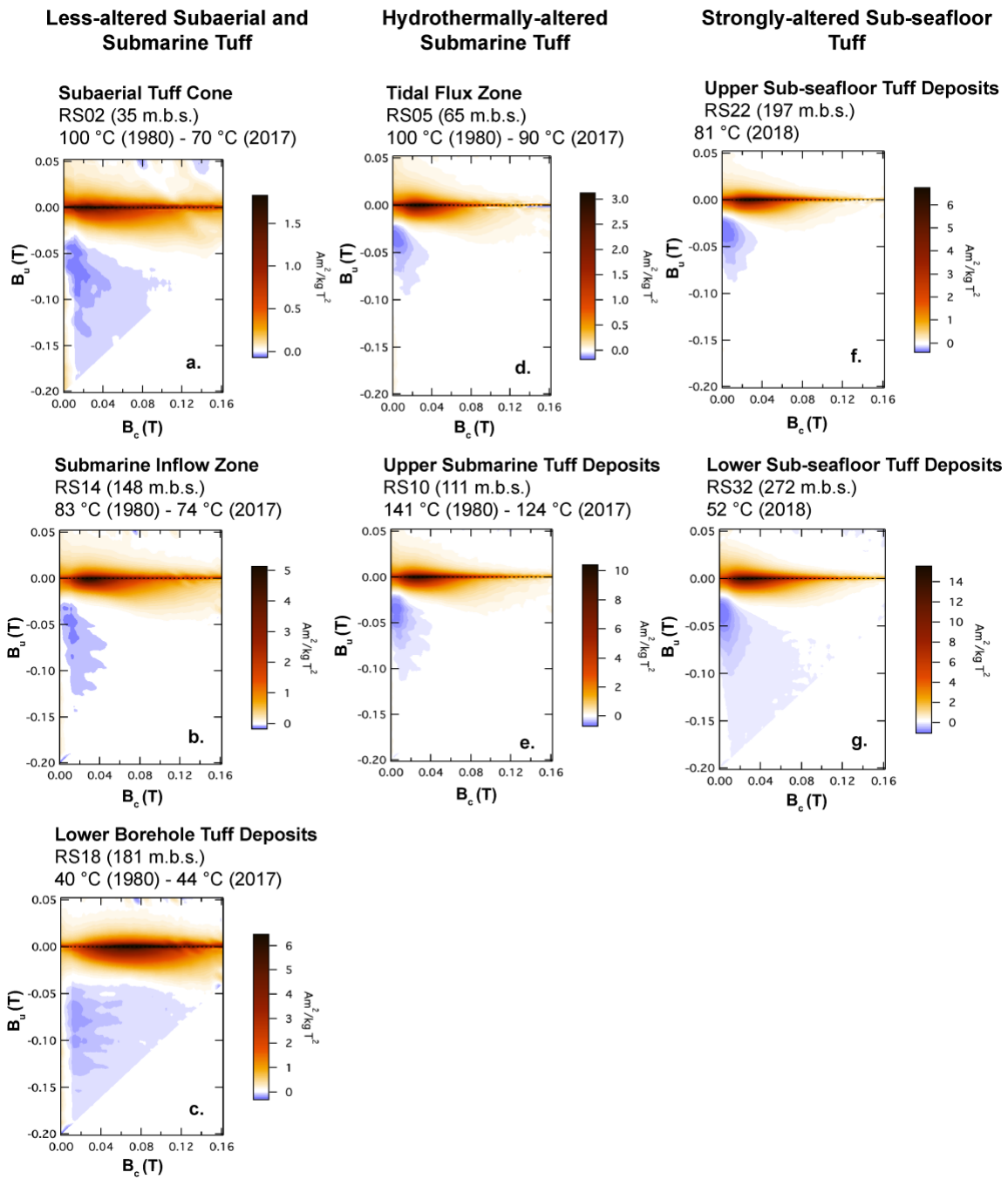


Figure 9: First-order reversal curve (FORC) diagrams for aliquots from the seven representative reference samples. Details of the FORC processing are provided in Section 3.5 and smoothing parameters for each diagram are provided in Table A2.

5 DISCUSSION

5.1 Petrographic and Material Descriptions

Our qualitative assessment of petrographic thin section scans reveals distinct differences in the extent of glass alteration and apparent connected porosity in the basaltic lapilli tuff samples (Figure 4). The less-altered lapilli tuff occurs in three alteration zones: the subaerial tuff cone (RS02; Figure 4a), the submarine inflow zone (RS14; Figure 4b), and the lower borehole tuff deposits (RS18; Figure 4c). Specimen RS18 was deposited near the cool pre-eruption seafloor, where temperature varied from 40 – 44 °C between 1980 and 2017. Specimen RS18 is also the only sample that contained abundant very weakly-altered glass pyroclasts devoid of palagonitized rinds at this scale of observation (Figure 4c). RS18 is the least altered sample of the seven representative reference samples in our study. We hypothesize that RS18 is the only specimen to contain the original, unaltered primary magnetic remanence carrying minerals. Specimens RS02 and RS14 show relatively minimal alteration, as determined by the presence of very weakly-altered vitric pyroclasts with palagonitized rinds. Specimen RS02 was deposited subaerially and was exposed to meteoric water; borehole temperatures varied from 100 – 70 °C between 1980 and 2017. Specimen RS14 comes from a submarine inflow zone; borehole temperatures varied from 83 – 74 °C between 1980 and 2017. We hypothesize that these less-altered zones of the hydrothermal system are, in part, a result of the exposure to relatively cool meteoric water, seawater, or both.

The tidal flux zone and upper submarine hydrothermal zone, represented by specimens RS05 and RS10 show more alteration than specimens RS02, RS14, and RS18. Here, alteration is determined by an absence of fresh-to-weakly-altered glass pyroclasts; RS05 contains no apparent glass and the scanned area of RS10 shows one glass pyroclast with a thick palagonitized rind (Figures 4d, e). Specimen RS05 was exposed to a mixture of meteoric water and seawater; borehole temperatures at this position varied from 100 – 90 °C between 1980 and 2017. Specimen RS10 represents the maximum temperature zone of the hydrothermal system; borehole temperatures varied from 141 – 124 °C between 1980 and 2017. In contrast to the less-altered specimens, we hypothesize that the greater extent of glass alteration observed in specimens RS05 and RS10 is strongly linked to interaction with water at higher temperatures (Jakobsson & Moore, 1986; Jackson et al., 2019a; Jackson, 2020).

The upper and lower sub-seafloor tuff deposits, represented by specimens RS22 and RS33 from the SE-03 core, respectively, come from more strongly-altered zones. The samples from Core SE-03 contain strongly-altered and highly vesicular glass pyroclasts and overall the tuff specimens appear to have a high connected porosity (Figures 4f, g). Temperatures of water samples collected in 2018 reveal temperatures of 81 °C for specimen RS22 and 52 °C for specimen RS32 (Kleine et al., in press). Core SE-03 traverses the deep central vent structure of the volcano (Figure 2) through deposits that were possibly remobilized during fluctuating explosive activity (Moore, 1985). Fluid compositions may be different from samples from Core SE-02b, because the deposits are farther from the periphery of the volcano and may have limited access to seawater. Hence, although the samples from Core SE-03 show the greatest extent of alteration, it is

difficult to compare the alteration pathways of samples from Core SE-02b to those from Core SE-03.

Palagonitization is a poorly-defined process that refers to the hydrous alteration of volcanic glass and the incremental production of authigenic minerals, principally clay minerals and zeolites, through volcanic glass alteration (Stroncik & Schmincke, 2002). Palagonitization at Surtsey was first observed on the surface of Surtsey in 1969 (Jakobsson, 1972) and the zones of lithified, palagonitized tuff grew until they encompassed much of the subaerial tephra deposits of Surtur and Surtungur by 2006 (Ólafsson & Jakobsson, 2009; Moore & Jackson, 2020). Much of the upper submarine lapilli tuff of the 1979 SE-01 drill core had undergone intensive palagonitic alteration within the twelve years after eruptions terminated (Jakobsson & Moore, 1986). In the samples from the 2017 Core SE-02b investigated here, only the weakly-consolidated specimen from the lowermost borehole tuff deposits (RS18), deposited near the cool sedimentary rocks of the pre-eruption seafloor, shows very weakly-altered vitric pyroclasts and minimal palagonitization processes (Figure 4c). The strongly-altered vitric pyroclasts of the 2017 SE-03 core samples from the sub-seafloor deposits reflect the most intensively-altered zones investigated in this study (Figures 4f, g).

5.2 Paleomagnetism of Core SE-02b

We interpret the steep low-coercivity component as a drilling overprint (Component 1 in Table 2). Such overprints are common in many drilling operations of sediments and igneous rocks (*e.g.*, Acton et al., 2002; Bowles, 2007). The drilling overprint is typically a viscous isothermal remanent magnetization produced from piston and rotary coring and here we use it to refer to any magnetic overprint acquired by the

cores during drilling operations. Because the Surtsey cores were not azimuthally oriented, magnetic declination is highly variable. Instead of calculating a Fisher mean ChRM direction, we calculated the maximum likelihood estimate of the inclination of the ChRM directions (Component 2 in Table 2) of $77 \pm 2^\circ$, using the Arason and Levi (2010) method. The expected magnetic inclination at Surtsey at the time of eruption in 1963 is 75.5° (International Geomagnetic Reference Field, 13th Generation Calculator). The calculated and expected inclination values overlap at 95 % confidence; we conclude that the tuff deposits record the paleomagnetic field direction with high fidelity (Figure 10).

5.3 Magnetic Mineral Composition and its Variability

We measured several magnetic parameters in the full suite of reference samples that are sensitive to iron oxide stoichiometry. The most useful parameters include: saturation magnetization, magnetic susceptibility, magnetic coercivity, the median destructive field, S100, and S300 (Figure 5, Table A1). Figure 5 and Table A1 reveal minor changes in saturation magnetization with depth. Slight changes occur in bulk magnetic susceptibility with depth: the lowest susceptibility occurs in the tidal flux zone, the submarine inflow zone, and the lower borehole tuff deposits of the SE-02b core. Susceptibility peaks in the lower sub-seafloor tuff deposits of the SE-03 core. There are also changes in magnetic coercivity and median destructive field with depth. Notably, coercivity peaks in the relatively weakly-altered lapilli tuff samples from the subaerial tuff cone, submarine inflow zone, and lower borehole tuff deposits. These observations are corroborated by the S100 values. Low S100 values are in the subaerial tuff cone, submarine inflow zone, and lower borehole tuff deposits, suggesting a relatively low

concentration of magnetically soft minerals. There are no distinct changes in S300 downcore.

It is difficult, however, to use these parameters alone to accurately assess magnetic mineral composition, because many different combinations of minerals produce similar bulk measurement values; that is, these measurements often produce non-unique results at the precision that is needed in this study (Dunlop & Özdemir, 1997; Dubrovine & Tarduno, 2006; Roberts et al., 2018). For example, Dunlop and Özdemir (1997) showed that magnetic coercivity and magnetic saturation will produce non-unique solutions that strongly depend on the precise degree of oxidation (z) and Ti_{4+} substitution (x) (the former also depending on anisotropy type). Without knowledge of precise x and z values, assessing magnetic mineral composition from these bulk magnetic parameters alone is challenging. Instead, we use temperature dependence of magnetic susceptibility ($\kappa(T)$ curves) of the seven representative reference samples to interpret the magnetic mineral composition.

In all specimens except RS14 and RS18, continuous heating-cooling $\kappa(T)$ curves show an inferred Curie temperature of the original magnetic phase between 300 – 450 °C (Figures 6a, d-g). A second magnetic phase, indicated by a second ‘hump’ in the heating curve between ~450 – 550 °C, indicates an even higher Curie temperature near 580 °C (Figures 6b, d-g). A typical result, illustrated in samples RS02, RS05, RS10, and RS22 (Figures 6a, d-f), includes a broad hump between 150 – 350 °C, with a decrease in magnetic susceptibility occurring around 350 °C. Following definitions by Kontny and Grothaus (2017) and Bilardello (2020), this phenomenon is characteristic of maghemite and has been termed the “maghemite bump.” This behavior is common across rock types

and the initial increase in magnetic susceptibility of the original magnetic phase is attributed to the annealing of crystallographic stresses in the maghemite rim around a magnetite core (Bilardello, 2020). We also see a ‘hump’ in the $\kappa(T)$ curve for specimen RS32 (Figure 6g), but the increase in magnetic susceptibility is much greater and the inferred Curie temperature extends to slightly higher temperatures (~ 400 °C). We interpret this hump as the Hopkinson peak of titanomaghemite (Özdemir, 1987; Doubrovine & Tarduno, 2006). The weakly-altered submarine inflow zone (RS14) and lower borehole tuff deposits (RS18) do not show the characteristic maghemite bump nor the Hopkinson peak of titanomaghemite (Figures 6b, c).

The second hump in the heating curves can indicate the beginning of titanomaghemite inversion (most notably in Figures 6b, e) (Özdemir, 1987; Doubrovine & Tarduno, 2006). Specifically, the temperature at which inversion begins is marked by the ascending shoulder of the second hump in the heating curve (Doubrovine & Tarduno, 2006). The inversion onset temperatures are between 450 – 550 °C for RS05, RS10, RS14, RS22, and RS32 (Figures 6b, d-g). Most notably, the inversion temperatures calculated for specimens RS10 and RS14 are consistent with results from Özdemir (1987) and Doubrovine and Tarduno (2006). Keefer and Shive (1980) and Doubrovine and Tarduno (2004) used these inversion temperatures to estimate the extent of oxidation (z) and showed that the inversion onset temperature of titanomaghemites increases with increasing oxidation state. These studies report inversion temperatures ranging from ~ 250 °C for slightly oxidized titanomagnetites (TM60) to greater than 500 °C for more highly oxidized samples. Moreover, Özdemir (1987) measured the dependence of inversion temperature on the initial degree of oxidation (z) for TM60 titanomaghemites (where $x =$

0.6) and found that inversion temperatures fall in the range 250 – 460 °C for $0.2 < z < 0.9$, respectively. Inversion onset temperatures between ~450 – 460 °C in both the upper submarine tuff deposits (RS10; Figure 6e) and submarine inflow zone (RS14; Figure 6b) might suggest high oxidation states, where $z \approx 0.9$. This result is similar to findings by Grommé et al. (1979) and Grommé (1982) (Figures 6b, e). However, the Özdemir (1987) studies derived z values using specimens of TM60 titanomaghemite. Without precise estimates of x values of the seven representative reference samples, a direct comparison, and therefore an accurate estimate of z , cannot be made. A less ambiguous measurement, such as low-temperature remanence or chemical composition data from ion microprobe analyses, for example, should be used to accurately quantify the x parameter (Dobrovine & Tarduno, 2004).

Nagata (1961) and O'Reilly (1984) measured the dependence of Curie temperature on the extent of Ti_{4+} substitution (x) in (titano)magnetite samples where $0.0 < x < 1.0$ in $\text{Fe}_{3-x}\text{Ti}_x\text{O}_4$. These studies found that Curie temperatures between 300 – 430 °C correspond to x values ranging from ~0.5 – 0.2, respectively. Curie temperatures in this range are measured in specimens RS02, RS05, RS10, RS22, and RS32; these correspond to $x \approx 0.5$ in the subaerial tuff cone, tidal flux zone, and upper submarine tuff deposits and $x \approx 0.2$ in both the upper and lower sub-seafloor tuff deposits (Figures 6 and 7a, d-g).

Our progressive heating-cooling $\kappa(T)$ curves (Figure 7) corroborate these interpretations. RS18 is the only specimen that is consistent with magnetite as the dominant magnetic remanence carrier. This specimen is from the very weakly-altered lower borehole tuff deposits. The original magnetic phase of RS18 has a Curie

temperature near 580 °C (Figure 7c). For all specimens except RS18, progressive heating-cooling curves are irreversible after 300 – 400 °C, Curie temperatures progressively increase with each heating step, and magnetic susceptibility gradually increases with each heating step up to 700 °C. These characteristics are most notable in specimens RS02, RS10, RS22, and RS32 (Figures 7a, e, f, g). Previous studies suggest that titanomaghemite is indicated by irreversibility in thermomagnetic curves in specimens that have two or more magnetic phases and in which the Curie point of a low-temperature phase rises progressively with temperature (Doubrovine & Tarduno, 2004, 2005, 2006; Coe et al., 2014). This phenomenon can indicate progressive alteration of titanomaghemite or low-temperature oxidation of titanomagnetite (Coe et al., 2014). For all other specimens (*i.e.*, RS02, RS05, RS10, RS14, RS22, and RS32), the presence of magnetite in unheated samples cannot be ruled out from these experiments, but Curie temperatures between 250 – 400 °C in the initial heating-cooling cycles suggest the presence of metastable iron oxide products. Magnetite could have formed through heating during the measurement (Figures 7a, b, d-g).

The presence of titanomagnetite, titanomaghemite, or both as the principal magnetic remanence carriers is corroborated by previous studies of 1979 Surtsey tuff samples by Grommé et al. (1979) and Grommé (1982). These studies presented results from a suite of magnetic measurements, including continuous thermomagnetic curves of remanence, on specimens at 53.3 m.b.s. and 107.5 m.b.s. from the 1979 Core SE-01. These stratigraphic positions directly parallel our SE-02b core samples and correspond to specimens RS05 and RS10, respectively. Grommé et al. (1979) and Grommé (1982) report markedly irreversible behavior in continuous temperature *vs.* remanence curves of

both specimens and, interestingly, they observe three maxima in the heating curve of the sample at 107.5 m.b.s. sample (similar to RS10 at 111 m.b.s.) (Figure 6e). They measured Curie temperatures at 250 ± 50 °C for the specimen at 53.3 m.b.s. and 350 ± 50 °C for the specimen at 107.5 m.b.s. With this information, they derived oxidation parameters for both specimens and concluded that $z = 0.8$ for the specimen at 53.3 m.b.s. and $z \approx 1.0$ for the specimen at 107.5 m.b.s. Although these studies report titanomagnetite, titanomaghemite, or both as the principal magnetic remanence carriers with potentially high oxidation states ($0.8 < z < 1.0$), they found that the Surtsey deposits recorded the expected geomagnetic field inclination.

5.4 Magnetic Domain State and its Variability

Our results indicate that the dominant magnetic domain state of the majority of the magnetic remanence carriers is stable single domain. The squareness ratio (M_{rs}/M_s), frequency-dependent magnetic susceptibility (χ_{fd}), sigma hysteresis, and susceptibility of ARM (χ_{ARM}) all help identify the bulk magnetic domain state (Figure 5). The squareness ratio of SE-02b core samples is relatively high (0.43 – 0.49) near the less-altered zones and decreases (0.38 – 0.41) in the hydrothermally-altered zones of the volcano. Frequency-dependent magnetic susceptibility has minor peaks near the tidal flux zone and lower borehole tuff deposits, suggesting a higher concentration of superparamagnetic particles (grains <20 nm) in these zones. We would predict that samples with higher χ_{fd} values will have more positive sigma hysteresis (*i.e.*, wasp-waisted) values. We do measure positive sigma hysteresis values in the tidal flux zone, but sigma hysteresis values are negative in the lower borehole tuff deposits. Overall, the variation in sigma

hysteresis is minor with depth, suggesting minor changes in magnetic particle sizes with depth that probably do not substantially contribute to changes in magnetic remanence insofar as our sample collection represents the entire cored section. ARM susceptibility, which targets single domain magnetite, also has little variation with depth; χ_{ARM} values are lowest within and near the tidal flux zone. The values of these three parameters do show some variation with depth, but they are difficult to use alone to accurately assess the magnetic domain state (*e.g.*, Roberts et al., 2018). In contrast, FORC diagrams are ideally suited to identify different magnetic domain states in bulk samples (Roberts et al., 2014, 2019).

FORC diagrams for each of the seven representative reference samples show that the dominant magnetic domain state of the dominant magnetic remanence carriers is stable single domain (Figures 9a-g). The diagrams have prominent central ridges with distributed magnetic coercivities and spreading along the $B_u = 0$ axis. Each sample is also characterized by negative values in the $B_u < 0$ region, which is diagnostic of stable single domain (titano)magnetite/maghemite (Muxworthy et al., 2004; Newell, 2005; Zhao et al., 2017; Roberts et al., 2014, 2019). Specimens RS02, RS14, and RS18 also show contributions from superparamagnetic and multidomain grains, indicated by the spreading along the $B_u(T)$ axis near $B_c(T) = 0$ (Figures 9a-c). This observation is consistent with the higher χ_{fd} values in these zones (4th panel of Figure 5). We interpret differences in the peak contributions to magnetic coercivity distributions (from 30 – 85 mT) with depth in the cores to reflect changes in magnetocrystalline and shape anisotropies (Gee & Kent, 1995; Roberts et al., 2018).

The dispersion of the magnetic coercivity distributions along the central ridge of the FORC diagram will decrease as (titano)magnetite particle shapes change from uniaxial anisotropy to a more isotropic anisotropy (Muxworthy et al., 2004). Lower magnetic coercivities are often reported in particles with isotropic and cubic anisotropy because these grain shapes have low magnetocrystalline anisotropy (Gee & Kent, 1995; Tauxe et al., 2018). Grains with cubic anisotropy have four easy axes of magnetization (corresponding to eight ‘easy’ magnetization directions). Magnetic coercivity typically increases, however, in particles with uniaxial anisotropy because grains are strongly controlled by internal stress and have only one easy axis of magnetization (corresponding to two ‘easy’ magnetization directions). The switching field, or the energy required to move the magnetic remanence from one easy direction to another, increases with increasing uniaxial anisotropy. Uniaxial anisotropy is a function of grain size and shape, and it often reflects the presence of needle-shaped particles (Gee & Kent, 1995; Roberts et al., 2014). As such, specimens with dominant magnetic coercivities in the ~30 – 45 mT range, including RS02, RS05, RS10, RS14, RS22, and RS32 (Figures 9a, b, d-g), suggest a magnetization controlled by cubic or a more isotropic anisotropy. By contrast, specimen RS18 (Figure 9c) has a dominant magnetic coercivity of ~85 mT. We interpret this as a magnetization that is controlled by uniaxial and cubic anisotropy, consistent with findings by Muxworthy et al. (2004) and Smirnov (2006). The interpretation that we measured cubic anisotropy in all seven representative reference samples is also consistent with findings by Gee and Kent (1995), who suggested that cubic anisotropy may be the dominant anisotropy type that controls the magnetic remanence in young mid-ocean ridge basalts. Cubic anisotropy can explain the high M_{rs}/M_s values measured for all samples.

One potential explanation for the inferred magnetic grain-size reduction and shape transformation is though domain wall pinning. This may result from crystallographic imperfections such as lattice vacancies through the removal of Fe^{2+} by maghemitization, inclusions of titanium or aluminum, and dislocations (Petersen & Vali, 1987; Housden & O'Reilly, 1990; Lindquist et al., 2015; Roberts et al., 2018; Bilardello, 2020). The pervasiveness of these imperfections is strongly controlled by diffusion rates, which depend on temperature and the oxidation gradient (between the oxidized crystal surface and the crystal interior) (Bilardello, 2020). Maghemitization accelerates as altered glass pyroclasts dissolve and crack and expose the remanence-carrying iron oxides to higher fluid temperatures ($> 50\text{ }^{\circ}\text{C}$). In this way, maghemitization reduces the physical and magnetic grain-size of the iron oxides. In other words, the relatively high peak contribution to magnetic coercivity ($B_c = 85\text{ mT}$; Figure 9c) measured in the very-weakly altered specimen (RS18) probably reflects an assemblage of needle-shaped and cubic grains that experienced little-to-no reduction in grain size, shape transformation, or both. By contrast, the pronounced decrease in peak contributions to magnetic coercivity ($30\text{ mT} < B_c < 45\text{ mT}$) in all other specimens (RS02, RS05, RS10, RS14, RS22, and RS32) may reflect a reduction in, and transformation of, crystal size, grain-size, or both as a result of maghemitization. Our petrographic observations document glass alteration that could correspond to systematic changes in the coercivity distributions measured by FORCs. If grain-size reduction by domain-wall pinning and physical cracking of maghemite shells around the cores of magnetite crystals is the explanation for the variation in magnetic coercivity, then we should observe evidence of this in transmission electron microscopy and magnetic force microscopy.

5.5 Magnetic Mineral Alteration and its Variations

The integrated results of the diverse investigations of the seven selected reference samples indicate that cubic and more isotropic stable single domain titanomagnetite and titanomaghemite are the dominant magnetic remanence-carrying minerals in six of the seven alteration zones recorded by the Surtsey drill cores. The sole exception is specimen RS18 from the lowermost borehole tuff deposits. This result is informed by (1) differences in the temperature history experienced by each specimen (Figures 3b, c); (2) the observations of glass alteration and progressive palagonitization in thin section scans (Figure 4); (3) differences in the amount of connected porosity among tuff specimens (Figure 4); (4) thermomagnetic curves showing evidence of suppressed Curie temperatures, the maghemite bump, the Hopkinson peak, and titanomaghemite inversion (Figures 6 and 7); and (5) FORC diagrams showing grain size reduction and the potential transformation from uniaxial and cubic anisotropy to a more isotropic anisotropy (Figure 9). Similar to studies by Tauxe and Staudigel (2004), Tauxe (2005), Bowles et al. (2005, 2011), and Wang et al. (2020), we hypothesize that the fresh volcanic glass hosted the original magnetic remanence-carrying iron oxides in the freshly erupted basaltic tephra. We directly observe alteration and palagonitization of glass pyroclasts in thin section scans in the subaerial tuff cone (RS02), the upper submarine tuff deposits (RS10), and the submarine inflow zone (RS14). Moreover, in the tidal flux zone (RS05) and both the upper and lower sub-seafloor tuff deposits (RS22 and RS32), we observe strongly-altered, opaque glass pyroclasts that are dark in color and highly vesicular with a moderately well-connected porosity. The principal magnetic remanence carriers in these same six zones are cubic to isotropic single domain titanomagnetite and titanomaghemite,

as indicated by thermomagnetic runs and FORC diagrams. In contrast, we observe an abundance of very weakly-altered glass pyroclasts with no palagonitized rind and a moderately well-connected porosity in the lower SE-02b borehole tuff deposits.

Thermomagnetic curves and FORC diagrams of the same sample indicates that the dominant magnetic remanence carriers are uniaxial and cubic stable single domain magnetite. This interpretation is consistent with other studies of oceanic basalts (Hodych & Matzka, 2004; Zhao et al., 2006; Bowles, 2011).

We interpret the observed remanence changes to reflect differences in the extent of alteration of the glassy component of the basaltic tephra produced through fluid-rock interactions, which result from complex interdependent variables, including changing temperatures, fluid compositions, and evolving porosity and permeability characteristics of the deposit. The fine scale studies of the progressive alteration of basaltic glass (Hay & Iijima, 1968; Stroncik & Schmincke, 2001, 2002; Walton & Schiffman, 2003; Pauly et al., 2011; Jackson et al., 2019b) may provide a context for further insight into the alteration rates of magnetic minerals in basaltic systems over variable temperatures, time scales, and environmental conditions.

Table 2: Demagnetization behavior and information on ChRM determinations for samples from Core SE-02b. Table includes information for both magnetization components (ChRM and low-coercivity overprint) including: reference sample number, median destructive field (MDF), intensity of demagnetization steps used to estimate magnetic inclination, total number of demagnetization steps used in estimations (N), maximum angular deviation (MAD), magnetic inclination, and whether it was used in calculating the mean magnetic inclination (yes or no).

Core SE-02b													
Component 1 - Overprint								Component 2 - ChRM					
Sample	MDF (mT)	Demagnetization Steps (mT)	N	MAD	Inclination (°)	Declination (°)	Used in mean?	Demagnetization Steps (mT)	N	MAD	Inclination (°)	Declination (°)	Used in mean?
RS-1	80.0	5-15	4	19.8	38.6	252.4	n	70-230	8	1.7	66.9	295.9	n
RS-2	87.9	0-25	8	9.6	77.6	61.3	y	0					n
RS-3	57.6	0-40	11	5	55.9	200.6	y	70-260	9	4.1	52.7	200.6	n
RS-4	63.7	0-35	10	12.1	75.5	268.4	y	60-230	9	2.8	79.6	263.3	y
RS-5	41.4	0-20	7	20.1	72.0	262.7	n	80-150	4	1.9	83.2	300.8	n
RS-6	51.7		0				n	0					n
RS-7	50.7	10-25	4	11.5	77.4	216.9	y	80-150	4	2.7	81.2	194.7	y
RS-8	39.5	0-30	9	3.8	72.8	117.0	y	35-125	8	0.8	73.2	130.0	y
RS-9	26.5	0-15	6	11.9	35.5	45.6	y	50-100	5	3.8	77.7	40.1	y
RS-10	45.8	7.5-30	6	3.9	74.2	125.1	y	80-125	4	2.4	76.5	162.6	y
RS-11	46.4	0-20	7	15.2	70.0	318.2	n	70-125	4	0.6	73.8	325.9	y
RS-12	43.0	0-30	9	2.8	78.2	194.9	y	80-125	4	1.7	76.9	183.1	y
RS-13	49.4	20-35	4	7.2	64.8	80.5	y	80-150	4	1.7	74.4	89.9	y
RS-14	94.1	0-30	9	8.5	47.8	16.4	y	60-230	9	0.7	74.2	39.4	y
RS-15	28.9		0				n	0					n
RS-16	67.5	0-35	10	7.3	83.9	352.4	y	80-150	4	1	79.7	12.1	y
RS-17	59.9	7.5-25	5	10.2	76.5	187.7	y	80-150	4	1.2	72.8	125.2	y
RS-18	68.2	2.5-35	9	16.8	57.8	80.6	n	100-150	4	3.2	75.4	60.3	y

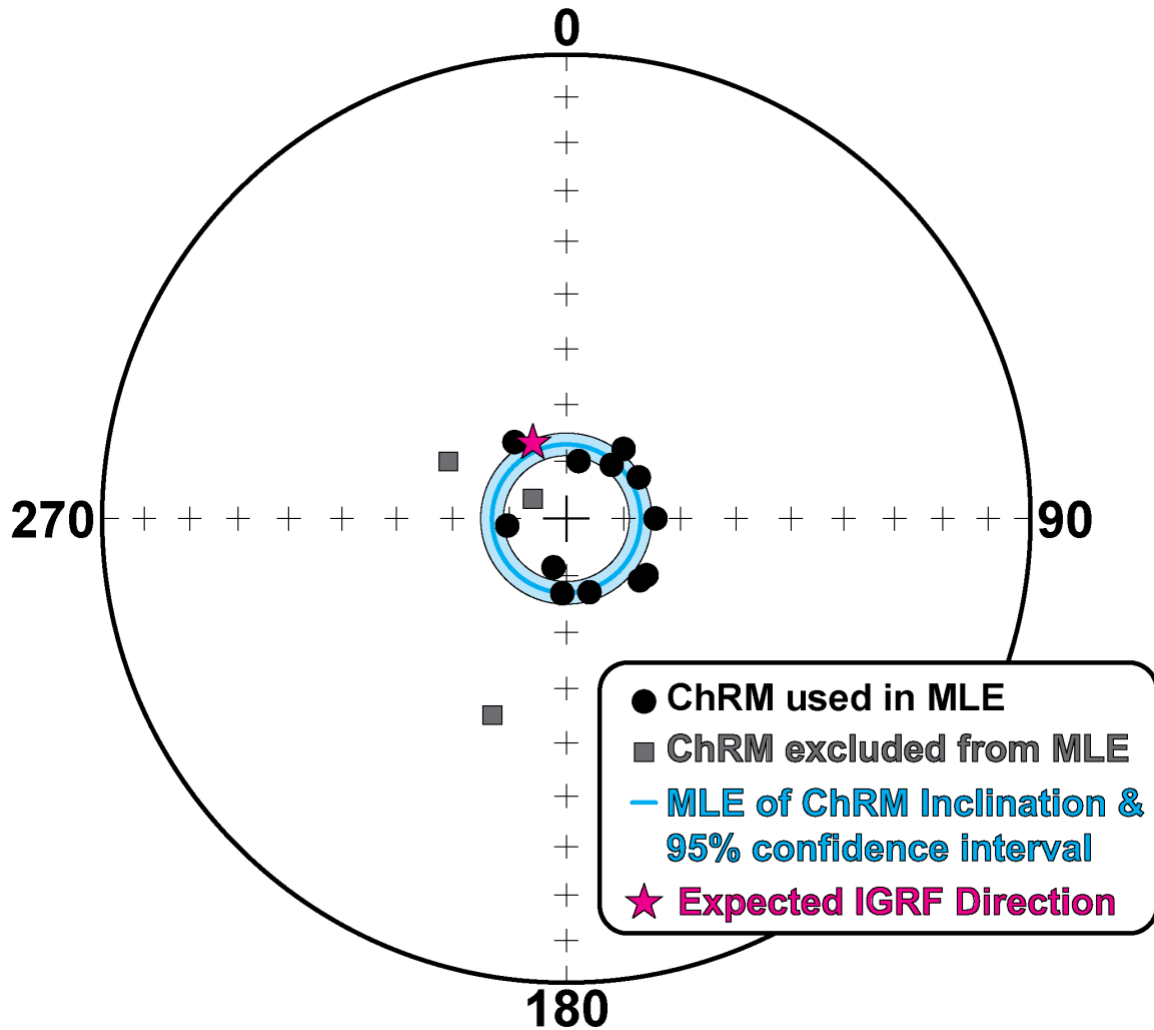


Figure 10: Stereonet showing paleomagnetism of samples from Core SE-02b. Characteristic remanent magnetization (ChRM) directions used to calculate the maximum likelihood estimate (MLE) of magnetic inclination are shown as black circles, whereas ChRM directions excluded from MLE determinations are shown as gray squares. The MLE of ChRM inclination with the 95% confidence interval is shown by the dark blue circle and light blue ring, respectively. The expected magnetic inclination during the time of eruption at Surtsey in 1963 (obtained from the International Geomagnetic Reference Field (IGRF)) is shown by the magenta star.

6 CONCLUSIONS

We report several important and foundational insights that provide a new investigative framework for studying the mineral magnetism of very young subaerial to submarine basaltic hydrothermal systems. (1) The magnetic properties of magnetic remanence carrying iron oxides can change over a few decades through fluid-rock interactions and elevated temperatures as they undergo alteration through Ti^{4+} substitution and maghemitization. (2) A correlation exists between the presence of fresh to weakly-altered volcanic glass and the progressive alteration of volcanic glass with magnetic properties: more strongly-altered glass pyroclasts correlate with greater changes to magnetic remanence characteristics with respect to the least altered sample. (3) The transformation from magnetite to titanomagnetite, titanomaghemite, or both produces a measurable transformation of magnetic grain shape and reduction in magnetic domain size that we suggest can be measured using conventional FORC diagrams. (4) Although considerable iron oxide alteration has occurred, the 2017 Surtsey drill cores record the paleomagnetic field direction during the time of eruption with high fidelity.

The subaerial tuff cone (RS02), the submarine inflow zone (RS14), and the lower borehole tuff deposits (RS18) show the least amount of alteration of the seven representative reference samples. Specimen RS18 was deposited near the cool pre-eruption seafloor, where temperature varied from 40 – 44 °C between 1980 and 2017. Specimen RS18 appears to be the best record of the original magnetic properties and the

only sample to carry the original, unaltered magnetic phase of the freshly erupted tephra. We reach this interpretation based on the observation of abundant very weakly-altered glass pyroclasts with no palagonitized rinds, an original Curie temperature near 580 °C, and a magnetic remanence controlled by uniaxial and cubic anisotropy with a peak contribution to the magnetic coercivity distribution in a FORC diagram near $B_c = 85$ mT.

Specimens RS02 and RS14 show some alteration progress, determined from the presence of weakly-altered vitric pyroclasts with palagonitized rinds. This is corroborated by rock magnetic measurements and is indicated by irreversibility in thermomagnetic curves that start at or below 400 °C, suppressed Curie temperatures, and a reduction and transformation of the magnetic grain-size with peak contributions to the magnetic coercivity distribution of FORC diagrams between $40 \text{ mT} < B_c < 45 \text{ mT}$. In 1980, borehole temperatures indicate that RS02 experienced boiling temperatures in meteoric water at 100 °C but temperatures decreased gradually to 70 °C in 2017. Borehole temperatures and geophysical downhole logs (Jakobsson & Moore, 1986; Jackson et al., 2019a) indicate that RS14 was exposed to a cooler mixture of meteoric water and seawater between 83 – 74 °C in 1980 and 2017, respectively.

In contrast, the specimens from the tidal flux zone (RS05) and upper submarine hydrothermal zone (RS10) show more intensive alteration than specimens RS02, RS14, and RS18. Specimens RS05 and RS10 contain no visible fresh glass. Rock magnetic measurements are consistent with the petrographic observations of greater alteration. They reveal a greater reduction and transformation of the magnetic grain-size, inferred from the lower peak contributions to the magnetic coercivity distribution of FORC diagrams, irreversibility in thermomagnetic curves starting at or below 400 °C, and

suppressed Curie temperatures. In 1980, borehole temperatures indicate that RS05 experienced boiling temperatures at from 100 °C and temperatures decreased to 90 °C in 2017. Sample RS10, in the maximum temperature zone of the hydrothermal system, is from a position in the borehole that had temperatures of 141 °C in 1980 that decreased to 124 °C in 2017. These results indicate that the natural, progressive alteration of the magnetic remanence carrying iron oxides is dependent on temperature and fluid-rock interactions. However, several alteration pathways potentially exist that produce the observed changes to the magnetic properties of the iron oxides hosted in the tephra.

Samples RS22 and RS32 occur in the upper and lower sub-seafloor tuff deposits of the inclined SE-03 borehole. Advanced alteration is indicated by strongly-altered glass pyroclasts. This is corroborated by rock magnetic results that reveal a reduction and transformation in grain-size with a peak contribution to the magnetic coercivity distribution of FORC diagrams near $B_c = 30$ mT, markedly irreversible thermomagnetic curves, and the characteristic Hopkinson peak of titanomaghemite. Fluid samples collected in 2018 gave temperatures at 81 °C for specimen RS22 and 52 °C for specimen RS32 (Kleine et al., in press). Core SE-03 traverses the deep central vent structure of the volcano through deposits that may have been re-mobilized through explosive activity.

Changes to the magnetic properties from the least altered sample, RS18, to the more strongly altered samples, RS02, RS14, RS05, RS10, RS22, and RS32, appear to be the result of differences in the diverse thermal histories and fluid compositions experienced by the relatively homogeneous basaltic tephra deposits in the volcano over the 50 years since eruptions terminated in 1967. We hypothesize that these magnetic mineralogical changes are controlled by fluid-rock interactions, which result from

complex interdependent variables, including changing temperatures, fluid compositions, and evolving porosity and permeability characteristics of the deposit. Future work should focus on: understanding how porosity and permeability evolve with alteration progress in the tuff deposits; rock-magnetic measurements that accurately quantify the oxidation parameter (z) and degree of Ti^{4+} substitution (x) to have a better constraint on the type and extent of alteration to the magnetic remanence carrying iron oxides; and situating the magnetic remanence carriers in a better-constrained mineralogical context by studying alteration progress to recognize how glass alteration and the production of authigenic minerals influence the changing the magnetic remanence characteristics of the basaltic tuff.

The work described here is one component of the multi-disciplinary SUSTSAIN drilling project at Surtsey that is characterizing abiotic and biotic processes active in the lithification and mineralization of the basaltic tephra and the changes in physical and material characteristics of the resulting basaltic tuff over decadal timescales (Jackson et al., 2019a). In this study, we investigated the temporal and spatial scales of fluid-rock (abiotic) interactions and temperatures on iron oxides and the physical and chemical changes that occur. It is possible that the maghemite-induced cracking of the crystal surface provides conduits into the more reduced cores of each iron oxide grain, thereby accelerating the redistribution of Fe^{2+} through fluid-rock interactions (*e.g.*, Krasa et al., 2005). Physical cracking of the maghemite shell, grain size reduction, and a corresponding increase in the surface area to volume ratio of iron oxides could potentially create energy-rich microhabitats for chemolithotrophic microbes that would induce accelerated maghemitization of the iron oxides. For example, Byrne et al. (2016) and

Carlut et al. (2010) showed the efficiency of magnetic mineral alteration (including grain size reduction and maghemitization) mediated by cultured chemolithoautotrophs. We may eventually be able to ask, what are the effects of fluid-rock-microbe (biotic) interactions on the magnetic fidelity of basaltic crust?

APPENDIX

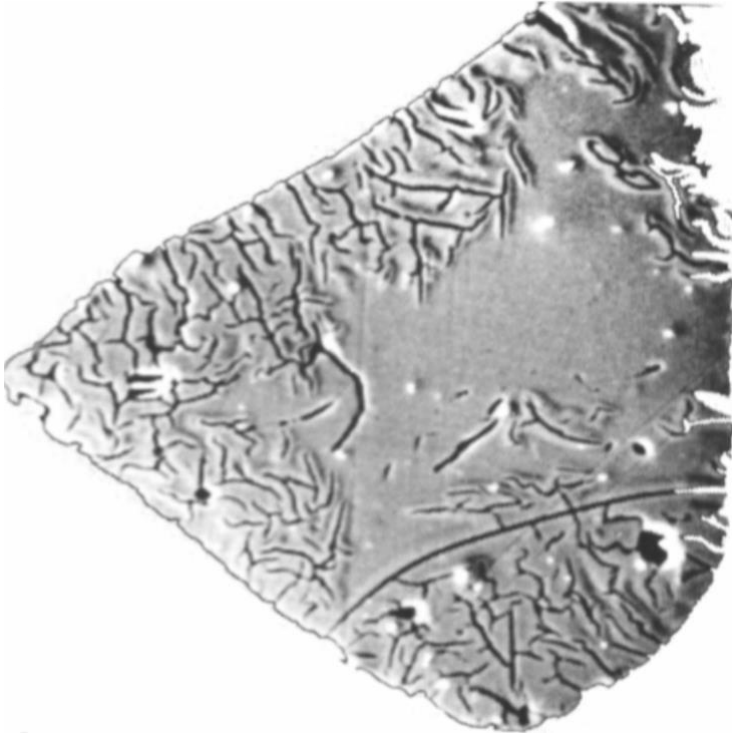


Figure A1: Maghemitization-induced surface cracking in a magnetite crystal $\approx 30 \mu\text{m}$ in size. The crystal lattice parameter of the oxidized maghemite surface layer is smaller than that of the unoxidized magnetite core and as a result, the oxidized surface layer stretches and cracks. (Figure from Dunlop & Özdemir, 1997).

Table A1: X_{lf} , low-frequency magnetic susceptibility; X_{hf} , high-frequency magnetic susceptibility; X_{fd} , frequency-dependent magnetic susceptibility; X_{fb} , adjusted χ_{fd} to be consistent with measurement on Bartington susceptibility meter. All reported magnetic susceptibilities are the mean of triplicate measurements of 7 cc sample cubes of known mass made using an AGICO MFK1 kappabridge. NRM, natural remanent magnetization; MDF, median destructive field; X_{ARM} , anhysteretic remanent magnetization. All reported magnetic remanence measurements were made using a JR6 spinner magnetometer. M_s , saturation magnetization; M_{rs} , saturation remanent magnetization; M_{rs}/M_s , squareness ratio; B_c , magnetic coercivity; B_{cr} , magnetic coercivity of remanence; B_{cr}/B_c magnetic coercivity ratio. All recorded hysteresis measurements were made on small sample chips (~0.1 g) using a Lakeshore Cryotronics/PMC Model 3900-4 vibrating sample magnetometer and exported from the Institute for Rock Magnetism Database.

Surtsey Reference Samples, 2017 Core					Kappabridge Susceptibility Bridge					JR6 Spinner Magnetometer			Vibrating Sample Magnetometer						
Reference Sample #	Sample ID		Vertical Depth (m.b.s.)	7 cc Cube Mass (g)	X_{lf} (x10E-7 (m ³ /kg))	X_{hf} (x10E-7 (m ³ /kg))	X_{fd} (x10E-6 SI)	X_{fd} (%)	X_{fb}	NRM Intensity (A/m)	MDF (mT)	X_{ARM}	Sample Mass (g)	M_s (Am/kg)	M_{rs} (Am/kg)	M_{rs}/M_s	B_c (mT)	B_{cr} (mT)	B_{cr}/B_c
SE-02B (HOLE C)																			
RS-1	5059-1-C-4-2A		22.66	17.576	3.8	3.6	0.2	5.26	-8.52	1.98E-01	80.0	2.91E-02	0.0916	1.75E-02	7.25E-03	4.13E-01	47.4	91.9	1.94
RS-2	5059-1-C-9-2		34.56	16.345	5.2	4.9	0.3	5.77	-11.62	2.46E-01	87.9	3.94E-02	0.0763	1.81E-02	7.78E-03	4.30E-01	47.2	90.2	1.91
RS-3	5059-1-C-13-2		44.44	17.781	6.1	5.8	0.3	4.92	-13.70	3.83E-01	57.6	2.80E-02	0.0985	3.22E-02	1.40E-02	4.34E-01	54.2	90.7	1.67
RS-4	5059-1-C-17-2		55.72	15.999	3.9	3.6	0.3	7.69	-8.63	1.63E-01	63.7	1.64E-02	0.0852	1.25E-02	4.91E-03	3.92E-01	34.7	70.0	2.02
RS-5	5059-1-C-22-2		65.11	17.004	3.8	3.6	0.2	5.26	-8.52	1.50E-01	41.4	7.85E-03	0.1228	1.46E-02	5.57E-03	3.82E-01	27.8	47.4	1.70
RS-6	5059-1-C-27-3		77.93	18.113	5.2	5.0	0.2	3.85	-11.74	4.22E-01	51.7	2.95E-03	0.0815	3.18E-02	1.35E-02	4.25E-01	35.5	56.4	1.59
RS-7	5059-1-C-30-2		86.20	15.425	5.1	4.9	0.2	3.92	-11.51	4.32E-01	50.7	1.53E-02	0.0608	6.43E-02	2.81E-02	4.36E-01	37.2	57.9	1.56
RS-8	5059-1-C-33-2A		92.34	16.228	4.3	4.1	0.2	4.65	-9.67	3.32E-01	39.5	8.84E-03	0.0607	1.74E-02	6.65E-03	3.81E-01	25.2	40.3	1.60
RS-9	5059-1-C-36-2		100.84	16.728	4.0	3.9	0.1	2.50	-9.09	3.61E-01	26.5	5.54E-03	0.085	1.39E-02	4.97E-03	3.56E-01	21.4	36.0	1.68
RS-10	5059-1-C-39-2		110.71	19.541	6.6	6.4	0.2	3.03	-14.97	1.07E+00	45.8	2.38E-02	0.1164	4.63E-02	1.87E-02	4.05E-01	32.6	54.1	1.66
RS-11	5059-1-C-42-3		120.33	20.236	7.8	7.4	0.4	5.13	-17.50	1.22E+00	46.4	2.99E-02	0.1014	6.26E-02	2.56E-02	4.09E-01	32.3	51.5	1.59
RS-12	5059-1-C-45-1		127.83	19.901	7.7	7.4	0.3	3.90	-17.38	1.31E+00	43.0	3.04E-02	0.1451	3.24E-02	1.18E-02	3.64E-01	26.3	45.3	1.72
RS-13	5059-1-C-49-3		138.17	17.178	6.2	6.0	0.2	3.23	-14.04	8.55E-01	49.4	2.55E-02	0.1069	4.07E-02	1.58E-02	3.88E-01	29.2	51.0	1.75
RS-14	5059-1-C-52-3		148.44	18.532	4.2	4.0	0.2	4.76	-9.44	4.21E-01	94.1	3.60E-02	0.1492	3.49E-02	1.49E-02	4.26E-01	48.0	76.8	1.60
RS-15	5059-1-C-55-3		157.01	18.810	5.7	5.4	0.3	5.26	-12.78	2.99E+00	28.9	7.31E-02	0.1252	8.52E-02	4.17E-02	4.89E-01	80.8	124.2	1.54
RS-16	5059-1-C-59-2A		165.40	19.682	5.9	5.3	0.6	10.17	-12.88	1.85E+00	67.5	6.01E-02	0.1643	3.19E-02	1.31E-02	4.11E-01	34.6	57.6	1.67
RS-17	5059-1-C-62-3		175.98	17.843	5.7	5.5	0.2	3.51	-12.89	1.55E+00	59.9	4.96E-02	0.092	3.04E-02	1.31E-02	4.30E-01	38.9	65.6	1.69
RS-18	5059-1-C-65-2A		180.65	16.531	4.0	3.8	0.2	5.00	-8.98	5.69E-01	68.2	3.11E-02	0.0588	5.48E-02	2.43E-02	4.44E-01	72.7	95.6	1.31
SE-03 (HOLE D)																			
			Inclined Depth (m.b.s.)																
RS-19	5059-1-D-73-3	220.35-220.70	180.47	19.008	11.9	11.6	0.3	2.52	-27.05	2.04E+00	51.5	6.79E-02	0.1077	3.81E-01	1.62E-01	4.24E-01	37.4	63.5	1.70
RS-20	5059-1-D-74-2A	220.35-220.70	181.07	18.638	7.1	6.8	0.3	4.23	-16.00	1.49E+00	47.5	1.53E-02	0.1122	2.12E-02	8.27E-03	3.89E-01	27.6	45.5	1.65
RS-21	5059-1-D-76-3	221.085-222.46	187.49	19.013	7.8	7.5	0.3	3.85	-17.61	1.68E+00	53.9	3.22E-02	0.1324	6.58E-02	2.58E-02	3.92E-01	34.8	60.1	1.73
RS-22	5059-1-D-82-4	221.085-222.46	198.73	18.262	6.1	5.9	0.2	3.28	-13.81	1.06E+00	46.6	2.19E-02	0.1211	2.90E-02	1.19E-02	4.08E-01	31.2	48.2	1.55
RS-23	5059-1-D-85-3	228.92-229.22	205.91	17.222	8.4	8.1	0.3	3.57	-18.99	1.70E+00	44.6	3.23E-02	0.1269	5.68E-02	2.17E-02	3.83E-01	26.6	43.7	1.64
RS-24	5059-1-D-88-2	242.65-243.015	212.03	15.126	6.6	6.3	0.3	4.55	-14.85	1.29E+00	51.9	3.01E-02	0.1272	1.35E-02	4.74E-03	3.52E-01	28.4	52.4	1.84
RS-25	5059-1-D-91-1	251.24-251.55	218.86	17.359	7.0	6.7	0.3	4.29	-15.77	1.19E+00	49.4	2.66E-02	0.1292	4.06E-02	1.50E-02	3.70E-01	28.1	50.5	1.80
RS-26	5059-1-D-94-4	258.88-259.255	228.62	14.879	5.7	5.5	0.2	3.51	-12.89	7.99E-01	52.9	1.39E-02	0.1165	5.00E-02	1.71E-02	3.43E-01	27.6	49.9	1.81
RS-27	5059-1-D-97-2A	267.225-267.575	235.11	21.733	10.4	10.0	0.4	3.85	-23.48	3.22E+00	64.5	9.82E-02	0.1805	8.28E-02	3.32E-02	4.01E-01	40.4	66.5	1.65
RS-28	5059-1-D-100-4	279.14-279.39	243.41	20.421	7.6	7.3	0.3	3.95	-17.15	1.96E+00	62.6	5.95E-02	0.1009	2.56E-01	9.66E-02	3.78E-01	24.1	36.2	1.50
RS-29	5059-1-D-103-1	287.07-287.42	248.81	19.231	6.0	5.7	0.3	5.00	-13.47	1.29E+00	62.7	3.24E-02	0.1009	5.24E-02	1.98E-02	3.78E-01	32.3	55.6	1.72
RS-30	5059-1-D-106-4	297.21-297.51	258.47	18.170	7.1	6.8	0.3	4.23	-16.00	1.46E+00	63.4	5.07E-02	0.076	4.99E-02	1.96E-02	3.93E-01	32.7	55.4	1.70
RS-31	5059-1-D-109-3	303.80-304.16	265.37	17.422	6.9	6.7	0.2	2.90	-15.66	1.54E+00	59.0	3.59E-02	0.1392	7.72E-02	3.05E-02	3.95E-01	44.3	80.4	1.81
RS-32	5059-1-D-112-2A	315.59-315.95	271.92	19.723	9.4	9.1	0.3	3.19	-21.30	3.04E+00	51.0	5.30E-02	0.1179	6.90E-02	2.71E-02	3.92E-01	31.1	51.9	1.67

Table A2: Fitting parameters used to process FORC diagrams using FORCinel version 3.06 with VARIFORC smoothing. Sc0, vertical ridge; Sb0, central ridge; Sc1, horizontal smooth; Sb1, vertical smooth; lamda-H, horizontal lamda; lamda-V, vertical lamda. All recorded FORC measurements were made on small sample chips (<0.5 g) using a Lakeshore Cryotronics/PMC Model 3900-4 vibrating sample magnetometer.

Fitting Parameters for First-Order Reversal Curve Diagrams							
Sample	RS02	RS05	RS10	RS14	RS18	RS22	RS32
Mass (g)	0.0763	0.1228	0.1110	0.1492	0.0469	0.1095	0.1179
Sc0	20	20	15	20	20	20	15
Sb0	5	5	5	5	5	5	5
Sc1	20	23	15	20	20	20	15
Sb1	20	23	15	20	20	20	15
lamda-H	0.1	0	0	0	0	0	0
lamda-V	0.1	0	0	0	0	0	0

REFERENCES

- Acton, G. D., Okada, M., Clement, B. M., Lund, S. P., & Williams, T. (2002). Paleomagnetic overprints in ocean sediment cores and their relationship to shear deformation caused by piston coring. *Journal of Geophysical Research*, 107, 2067. <https://doi.org/10.1029/2001jb000518>
- Alexandersson, T. (1970). The sedimentary xenoliths from Surtsey: marine sediments lithified on the sea floor. *Surtsey Research Progress Report*, 6, 101-116.
- Alexandersson, T. (1972). The sedimentary xenoliths from Surtsey: turbidites indicating shelf growth. *Surtsey Research Bulletin*, 5, 83-89.
- Arason, Þ., & Levi, S. (2010). Maximum likelihood solution for inclination-only data in paleomagnetism. *Geophysical Journal International*, 182, 753-771. <https://doi.org/10.1111/j.1365246X.2010.04671>
- ASTM C97/C97M-18: Standard Test Methods for Absorption and Bulk Specific Gravity of Dimension Stone. ASTM International, West Conshohocken, PA. https://doi.org/10.1520/C0097_C0097M-18
- Baldursson, S., & Ingadóttir, Á. (2007). Nomination of Surtsey for the UNESCO World Heritage List, Icelandic Institute of Natural History, Reykjavik.
- Bilardello, D. (2020). Practical Magnetism II: Humps and a Bump, the Maghemite Song. *The IRM Quarterly*, 30(1), 15-17.
- Bowles, J., Gee, J., Kent, D., Bergmanis, E., & Sinton, J. (2005). Cooling rate effects on paleointensity estimates in submarine basaltic glass and implications for dating young flows. *Geochemistry, Geophysics, Geosystems*, 6, Q07002. <https://doi.org/10.1029/2004GC000900>
- Bowles, J. (2007). Coring-related deformation of Leg 208 sediments from Walvis Ridge: Implications for paleomagnetic data. *Physics of the Earth and Planetary Interiors*, 161, 161-169. <https://doi.org/10.1016/j.pepi.2007.01.010>
- Bowles, J. A., Gee, J. S., Burgess, K., & Cooper, R. F. (2011). Timing of magnetite formation in submarine basaltic glass: a comparison of natural and synthetic samples with implications for geomagnetic paleointensity studies. *Geochemistry, Geophysics, Geosystems*, 6, Q07002. <https://doi.org/10.1029/2010GC003404>

- Butler, R. F. (1992). *Paleomagnetism: Magnetic Domains to Geologic Terranes*. Blackwell Scientific Publications, Boston.
- Byrne, J. M., van der Laan, G., Figueroa, A. I., Qafoku, O., Wang, C., Pearce, C. I., et al. (2016). Size dependent microbial oxidation and reduction of magnetite nano- and micro-particles. *Scientific Reports*, 6, 30969. <https://doi.org/10.1038/srep30969>
- Carlut, J., Benzerara, K., Horen, H., Menguy, N., Janots, D., Findling, N., et al. (2010). Microscopy study of biologically mediated alteration of natural mid-ocean ridge basalts and magnetic implications. *Journal of Geophysical Research: Biogeosciences*, 115, G00G11. <https://doi.org/10.1029/2009JG001139>
- Coe, R. S., Jarboe, N. A., Goff, M. L., & Petersen, N. (2014). Demise of the rapid-field-change hypothesis at Steens Mountain: The crucial role of continuous thermal demagnetization. *Earth and Planetary Science Letters*, 400, 302-312.
- Dearing, J. A., Dann, R. J. L., Hay, K., Lees, J. A., Loveland, P. J., Maher, B. A., et al. (1996). Frequency-dependent susceptibility measurements of environmental materials. *Geophysical Journal International*, 124, 228-240.
- Dobrovine, P. V., & Tarduno, J. A. (2004). Self-reversed magnetization carried by titanomaghemite in oceanic basalts. *Earth and Planetary Science Letters*, 222, 959-969.
- Dobrovine, P. V., & Tarduno, J. A. (2005). On the compositional field of self-reversing titanomaghemite: Constraints from Deep Sea Drilling Project Site 307. *Journal of Geophysical Research*, 110, B11104. <https://doi.org/10.1029/2005JB003865>
- Dobrovine, P. V., & Tarduno J. A. (2006). N-type magnetism at cryogenic temperatures in oceanic basalt. *Physics of the Earth and Planetary Interiors*, 157, 46-54.
- Dunlop, D. J., & Özdemir, Ö. (1997). *Rock Magnetism, Fundamentals and Frontiers*, Cambridge University Press, Cambridge.
- Egli, R., & Lowrie, W. (2002). Anhysteretic remanent magnetization of fine magnetic particles. *Journal of Geophysical Research*, 107(B10), 2209. <https://doi.org/10.1029/2001JB000671>
- Egli, R. (2009). Magnetic susceptibility measurements as a function of temperature and frequency I: Inversion theory. *Geophysical Journal International*, 177, 395-420. <https://doi.org/10.1111/j.1365-246X.2009.04081>
- Egli, R. (2013). VARIFORC: An optimized protocol for the calculation of non-regular first-order reversal curve (FORC) diagrams. *Global and Planetary Change*. <https://doi.org/10.1016/j.gloplacha.2013.08.003>
- Einarsson, P. (2008). Plate boundaries, rifts and transforms in Iceland. *Jökull*, 58, 35-58.

- Fabian, K. (2003). Statistical theory of weak field thermoremanence magnetization in multidomain particle ensembles. *Geophysical Journal International*, 155, 479-488.
- Finn, D. R., & Coe, R. S. (2016). A new protocol for three-axis static alternating field demagnetization of rocks. *Geochemistry, Geophysics, Geosystems*, 17, 1815-1822.
<https://doi.org/10.1002/2015GC006178>
- Gee, J., & Kent, D. (1995). Magnetic hysteresis in young mid-ocean ridge basalts: Dominant cubic anisotropy?. *Geophysical Research Letters*, 22, 551-554.
<https://doi.org/10.1029/95GL00263>
- Grommé, S., Mankinen, E. A., Marshall, M., & Coe, R. S. (1979). Geomagnetic paleointensities by the Thelliers' method from submarine pillow basalts: Effects of sea-floor weathering. *Journal of Geophysical Research*, 84, 3553-3575.
- Grommé, S. (1982). Origin of natural remanent magnetization of tephra from the 1979 Surtsey drill hole, Iceland. *Surtsey Research Progress Report*, 9, 111-116.
- Harrison, R. J., & Feinberg, J. M. (2008). FORCinel: An improved algorithm for calculating first-order reversal curve distributions using locally weighted regression smoothing. *Geochemistry, Geophysics, Geosystems*, 9, A05016.
<https://doi.org/10.1029/2008GC001987>
- Hay, R. L., & Iijima, A. (1968). Nature and origin of palagonite tuffs of the Honolulu Group on Oahu, Hawaii. In R. R. Coats, R. L. Hay, & C. A. Anderson (Eds.). *Studies in volcanology, Geological of Society America Memoir*, 116, 331-376.
<https://doi.org/10.1130/MEM116>
- Hodych, J. P., & Matzka, J. (2004). Saturation magnetostriction and its low-temperature variation inferred for natural titanomaghemites: implications for internal stress control of coercivity in oceanic basalts. *Geophysical Journal International*, 157, 1017-1026.
<https://doi.org/10.1111/j.1365-246X.2004.02231>
- Housden, J., & O'Reilly, W. (1990). On the intensity and stability of the natural remanent magnetization of ocean floor basalts. *Physics of the Earth and Planetary Interiors*, 64, 261-278.
- Hrouda, F. (2011). Models of frequency-dependent susceptibility of rocks and soils revisited and broadened. *Geophysical Journal International*, 187, 1259-1269.
<https://doi.org/10.1111/j.1365-246X.2011.05227>
- Jackson, M., & Solheid, P. (2010). On the quantitative analysis and evaluation of magnetic hysteresis data. *Geochemistry, Geophysics, Geosystems*, 11, Q04Z15.
<https://doi.org/10.1029/2009GC002932>
- Jackson, M. D. (2020). Petrographic and material observations of basaltic lapilli tuff,

- 1979 and 2017 Surtsey drill cores, Iceland. *Surtsey Research*, 14, 47-62.
- Jackson, M. D., Gudmundsson, M. T., Weisenberger, T. B., Rhodes, J. M., Stefánsson, A., Kleine, B. I., et al. (2019). SUSTAIN drilling at Surtsey volcano, Iceland, tracks hydrothermal and microbiological interactions in basalt 50 years after eruption. *Scientific Drilling*, 25, 35-46. <https://doi.org/10.5194/sd-25-35-2019>
- Jackson, M. D., Couper, S., Stan, C. V., Ivarsson, M., Czabaj, M. W., Tamura, N., et al. (2019). Authigenic mineral textures in submarine 1979 basalt drill core, Surtsey volcano, Iceland. *Geochemistry, Geophysics, Geosystems*, 20(7). <https://doi.org/10.1029/2019GC008304>
- Jakobsson, S. P. (1972). On the consolidation and Palagonitization on the Tephra of the Surtsey Volcanic Island, Iceland. *Surtsey Research Progress Reports*, 121-128.
- Jakobsson, S. P. (2000). Geological map of Surtsey, scale 1 V 5000, Icelandic Institute of Natural History and the Surtsey Research Society, Reykjavík.
- Jakobsson, S. P., & Moore, J. G. (1982). The Surtsey research drilling project of 1979. *Surtsey Research Progress Report*, 9, 76-93.
- Jakobsson, S. P., & Moore, J. G. (1986). Hydrothermal minerals and alteration rates at Surtsey volcano, Iceland. *Geological Society of America Bulletin*, 97, 648-659.
- Jakobsson, S. P., Gudmundsson, G., & Moore, J. G. (2000). Geological monitoring of Surtsey, Iceland, 1967–1998, *Surtsey Research*, 11, 99-108.
- Jakobsson, S. P., Thors, K., Vésteinsson, Á. T., & Ásbjörnsdóttir, L. (2009). Some aspects of the seafloor morphology at Surtsey volcano: the new multibeam bathymetric survey of 2007. *Surtsey Research*, 12, 9-20.
- Keefer, C. M. & Shive, P. N. (1980). Titanomagnetites: conditions for oxidation, influence of rhombohedral phases, and temperature of inversion. *Earth and Planetary Science Letters*, 51, 199-205.
- Kleine, B. I., Stefánsson, A., Kjartansdóttir, R., Prause, S., Weisenberger, T. B., Reynolds, H. I., et al. (2020). The Surtsey volcano geothermal system: an analogue for seawater-oceanic crust interaction with implications for the elemental budget of the oceanic crust. *Chemical Geology*, in press.
- Kontny, A., & Grothaus, L. (2017). Effects of shock pressure and temperature on titanomagnetite from ICDP cores and target rocks of the El'gygytgyn impact structure Russia. *Studia Geophysica et Geodaetica*, 61, 162-183.
- Krása, D., Shcherbakov, V. P., Kunzmann, T., & Petersen, N. (2005). Self-reversal of remanent magnetization in basalts due to partially oxidized titanomagnetites. *Geophysical Journal International*, 162, 115-136. <https://doi.org/10.1111/j.1365-246X.2005.02656>

Krásá, D., & Matzka, J. (2007). Inversion of titanomaghemite in oceanic basalt during heating. *Physics of the Earth and Planetary Interiors*, 160, 169-179.

Lindquist, A. K., Feinberg, J. M., Harrison, R. J., Loudon, J. C., & Newell, A. J. (2015). Domain wall pinning and dislocations: Investigating magnetite deformed under conditions analogous to nature using transmission electron microscopy. *Journal of Geophysical Research: Solid Earth*, 120, 1415-1430.
<https://doi.org/10.1002/2014JB011335>

Liu, Q., Deng, C., Yu, Y., Torrent, J., Jackson, M. J., Banerjee, S. K., et al. (2004). Temperature dependence of magnetic susceptibility in an argon environment: implications for pedogenesis of Chinese Loess/palaeosols. *Geophysical Journal International*, 161, 102-112.

Liu, Q., Roberts, A. P., Torrent, J., Horng, C. S., & Larrasoána, J. C. (2007). What do the HIRM and S-ratio really measure in environmental magnetism?. *Geochemistry, Geophysics, Geosystems*, 8, Q09011. <https://doi.org/10.1029/2007gc001717>

Lorenz, V. (1974). Studies of the Surtsey tephra deposits. *Surtsey Research Progress Report*, 7, 72-79.

Marteinsson, V., Klonowski, A., Reynisson, E., Vannier, P., Sigurdsson, B. D., & Ólafsson, M. (2015). Microbial colonization in diverse surface soil types in Surtsey and diversity analysis of its subsurface microbiota. *Biogeosciences*, 12, 1191-1203.
<https://doi.org/10.5194/bg-12-1191-2015>

Mayergoyz, I. D. (1986). Mathematical models of hysteresis, *IEEE Transactions on Magnetics*, MAG-22, 603-608.

McElhinny, M., & McFadden, P. (2000). *Paleomagnetism: Continents and Oceans*. Academic Press, San Diego.

McPhie, J., White, J. D. L., Gorny, C., Jackson, M., Gudmundsson, M., & Couper, S. (in press). Lithofacies from the 1963-1967 Surtsey eruption in SUSTAIN drill cores SE-2a, SE-2b and SE-03. *Surtsey Research*, 14. Accepted, 03/15/2020.

Moore, J. G. (1985). Structure and eruptive mechanisms at Surtsey Volcano, Iceland. *Geological Magazine*, 122(6), 649-661.

Moore, J. G., & Jackson, M. D. (2020). Observations on the structure of Surtsey. *Surtsey Research*, 14, 33-45.

Muxworthy, A., Heslop, D., & Williams, W. (2004). Influence of magnetostatic interactions on first-order-reversal-curve (FORC) diagrams: a micromagnetic approach. *Geophysical Journal International*, 158, 888-897.

<https://doi.org/10.1111/j.1365-246X.2004.02358>

Nagata, T. (1961). *Rock Magnetism*, 2nd ed., Maruzen, Tokyo.

Newell, A. J. (2005). A high-precision model of first-order reversal curve (FORC) functions for single-domain ferromagnets with uniaxial anisotropy. *Geochemistry, Geophysics, Geosystems*, 6, Q05010. <https://doi.org/10.1029/2004GC000877>

O'Reilly, W. (1984). *Rock and Mineral Magnetism*, Blackie Academic and Professional, New York.

Ólafsson, M., & Jakobsson, S. P. (2009). Chemical composition of hydrothermal water and water-rock interactions on Surtsey volcanic island: A preliminary report. *Surtsey Research*, 12, 29-38.

Otake, T., Wesolowski, D. J., Anovitz, L. M., Allard, L. F., & Ohmoto, H. (2010). Mechanisms of iron oxide transformation in hydrothermal systems. *Geochimica et Cosmochimica Acta*, 74, 6141-6156.

Özdemir, Ö. (1987). Inversion of titanomaghemites. *Physics of the Earth and Planetary Interiors*, 46, 184-196.

Pauly, B. D., Schiffman, P., Zierenberg, R. A., & Clague, D. A. (2011). Environmental and chemical controls on palagonitization. *Geochemistry, Geophysics, Geosystems*, 12, Q12017. <https://doi.org.ezproxy.lib.utah.edu/10.1029/2011GC003639>

Petersen, N., & Vali, H. (1987). Observation of shrinkage cracks in ocean floor titanomagnetites. *Physics of the Earth and Planetary Interiors*, 46, 197-205.

Pike, C., & Fernandez, A. (1999). An investigation of magnetic reversal in submicron-scale Co dots using first order reversal curve diagrams. *Journal of Applied Physics*, 85, 6668-6676.

Prause, S., Weisenberger, T. B., Cappelletti, P., Grimaldi, C., Rispoli, C., Jónasson, K., et al. (2020). Alteration progress within the Surtsey hydrothermal system, SW Iceland – A time-lapse petrographic study of cores drilled in 1979 and 2017. *Journal of Volcanological and Geothermal Research*, 106754. <https://doi.org/10.1016/j.jvolgeores.2019.106754>

Reynisson, R. F., & Jakobsson, S. P. (2009). Xenoliths of exotic origin at Surtsey volcano, Iceland. *Surtsey Research Bulletin*, 12, 21-27.

Roberts, A. P., Pike, C. R., & Verosub, K. L. (2000). First-order reversal curve diagrams: A new tool for characterizing the magnetic properties of natural samples. *Journal of Geophysical Research*, 105, 461-475

Roberts, A. P., Heslop, D., Zhao, X., & Pike, C. R. (2014). Understanding fine magnetic particle systems through use of first-order reversal curve diagrams. *Reviews of Geophysics*, 52, 557-602. <https://doi.org/10.1002/2014RG000462>

Roberts, A. P., Tauxe, L., Heslop, D., Zhao, X., & Jiang, Z. (2018). A Critical Appraisal of the “Day” Diagram. *Journal of Geophysical Research: Solid Earth*, 123(4), 2618-2644. <https://doi.org/10.1002/2017JB015247>

Roberts, A. P., Hu, P., Harrison, R. J., Heslop, D., Muxworthy, A. R., Oda, H., et al. (2019). Domain state diagnosis in rock magnetism: Evaluation of potential alternatives to the Day diagram. *Journal of Geophysical Research: Solid Earth*, 124, 5286-5314. <https://doi.org/10.1029/2018JB017049>

Schipper, C. I., Jakobsson, S. P., White, J. D. L., Palin, J. M., & Bush-Marcinowski, T. (2015). The Surtsey Magma Series. *Scientific Reports*, 5, 11498. <https://doi.org/10.1038/srep11498>

Schipper, C. I., & White, J. D. L. (2016). Magma-slurry interaction in Surtseyan eruptions. *Geology*, 44, 195-198.

Smirnov, A. V. (2006). Memory of the magnetic field applied during cooling in the low-temperature phase of magnetite: Grain-size dependence. *Journal of Geophysical Research*, 111, B12S04. <https://doi.org/10.1029/2006JB004573>

Stroncik, N. A., & Schmincke, H.-U. (2001). Evolution of palagonite: Crystallization, chemical changes, and element budget. *Geochemistry, Geophysics, Geosystems*, 2(7). <https://doi.org/10.1029/2000GC000102>

Stroncik, N. A., & Schmincke, H.-U. (2002). Palagonite – A review. *International Journal of Earth Science*, 91(4), 680-697. <https://doi.org/10.1007/s00531-001-0238-7>

Tarduno, J. A., Duncan, R. A., Scholl, D. W., Cottrell, R. D., & Steinberger, B. (2003). The Emperor Seamounts: Southward Motion of the Hawaiian Hotspot Plum in Earth's Mantle. *Science*, 301, 1064. <https://doi.org/10.1126/science.1086442>

Tauxe, L., Mullender, T. A. T., & Pick, T. (1996). Potbellies, wasp-waists, and superparamagnetism in magnetic hysteresis. *Journal of Geophysical Research*, 101(B1), 571-583. <https://doi.org/10.1029/95JB03041>

Tauxe, L., & Staudigel, H. (2004). Strength of the geomagnetic field in the cretaceous normal Superchron: new data from submarine basaltic glass of the Troodos Ophiolite. *Geochemistry, Geophysics, Geosystems*, 5(2), Q02H06. <http://doi.org/10.1029/2003GC000635>

- Tauxe, L. (2005). Long-term trends in paleointensity: The contribution of DSDP/ODP submarine basaltic glass collections. *Physics of the Earth and Planetary Interiors*, 156, 223-241.
- Tauxe, L., Shaar, R., Jonestrask, L., Swanson-Hysell, N. L., Minnett, R., Koppers, A. A. P., et al. (2016). PmagPy: Software package for paleomagnetic data analysis and a bridge to the Magnetism Information Consortium (MagIC) Database. *Geochemistry, Geophysics, Geosystems*, 17, 2450-2463. <https://doi.org/10.1002/2016GC006307>
- Tauxe, L., Banerjee, S. K., Butler, R. F., & van der Voo, R. (2018). Essentials of Paleomagnetism, 5th Web Edition.
- Thórarinnsson, S., Einarsson, Th., Sigvaldason, G., & Elísson, G. (1964). The submarine eruption off the Vestmann Islands 1963–64. *Bulletin of Volcanology*, 29, 435-455.
- Thorarinsson, S. (1965). Some facts about the Surtsey eruption. *Nattúrufræðingurinn*, 35, 153.
- Thórarinnsson, S. (1967). Surtsey, The New Island in the North Atlantic, The Viking Press, New York.
- Thórarinnsson, S. (1969). Síðustu thaettir Eyjaelda (English summary: The last phases of the Surtsey eruption). *Náttúrufræðingurinn*, 38, 113-135.
- Thors, K. & Jakobsson, S. P. (1982). Two seismic reflection profiles from the vicinity of Surtsey, Iceland. *Surtsey Research Progress Report*, 9, 149-151.
- Walton, A. W., & Schiffman, P. (2003). Alteration of hyaloclastites in the HSDP 2 phase 1 drill core 1. Descriptions and paragenesis. *Geochemistry, Geophysics, Geosystems*, 4(5), 8709. <https://doi.org.ezproxy.lib.utah.edu/10.1029/2002GC000368>
- Wang, S., Chang, L., Wu, T., & Tao, C. (2020). Progressive dissolution of titanomagnetite in high-temperature hydrothermal vents dramatically reduces magnetization of Basaltic Ocean crust. *Geophysical Research Letters*, 47, e2020GL087578. <https://doi.org/10.1029/2020GL087578>
- Watkins, N. D. (1965). Frequency of extrusions of some Miocene lavas in Oregon during an apparent transition of polarity of geomagnetic field. *Nature*, 206, 801-803.
- Weisenberger, T. B., Gudmundsson, M. T., Jackson, M. D., Gorny, C., Türke, A., Kleine, B. I., et al. (2019). Operational Report for the 2017 Surtsey Underwater volcanic System for Thermophiles, Alteration processes and Innovative Concretes (SUSTAIN) drilling project at Surtsey Volcano, Iceland. *Geo Forschungs Zentrum (GFZ) German Research Centre for Geosciences*. <https://doi.org/10.2312/ICDP.5059.001>

Wilde, H., & Girke, H. (1959). Die messung der wahrscheinlichkeitsverteilung der Barkhausensprünge in einem ferromagnetikum. *Zeitschrift für angewandte Mathematik and Physik*, 11, 339-342.

Zhao, X., Roberts, A. P., Heslop, D., Paterson, G. A., Li, Y., & Li, J. (2017). Magnetic domain state diagnosis using hysteresis reversal curves. *Journal of Geophysical Research: Solid Earth*, 122, 4767-4789. <https://doi.org/10.1002/2016JB013683>